

Alma Mater Studiorum Università di Bologna
Archivio istituzionale della ricerca

Development of a lumping methodology for the analysis of the excited states in plasma discharges operated with argon, neon, krypton, and xenon

This is the final peer-reviewed author's accepted manuscript (postprint) of the following publication:

Published Version:

Souhair N., Magarotto M., Majorana E., Ponti F., Pavarin D. (2021). Development of a lumping methodology for the analysis of the excited states in plasma discharges operated with argon, neon, krypton, and xenon. PHYSICS OF PLASMAS, 28(9), 1-19 [10.1063/5.0057494].

Availability:

This version is available at: <https://hdl.handle.net/11585/833588> since: 2024-05-10

Published:

DOI: <http://doi.org/10.1063/5.0057494>

Terms of use:

Some rights reserved. The terms and conditions for the reuse of this version of the manuscript are specified in the publishing policy. For all terms of use and more information see the publisher's website.

This item was downloaded from IRIS Università di Bologna (<https://cris.unibo.it/>).
When citing, please refer to the published version.

(Article begins on next page)

Development of a lumping methodology for the analysis of the excited states in plasma discharges operated with argon, neon, krypton and xenon

N. Souhair,^{1, a)} M. Magarotto,^{2, b)} E. Majorana,^{1, c)} F. Ponti,^{1, d)} and D. Pavarin^{2, e)}

¹⁾*Alma Propulsion Laboratory, Department of Industrial Engineering, University of Bologna, Forlì, 47122, Italy.*

²⁾*Department of Industrial Engineering (DII), University of Padova, Padova, 35131, Italy.*

(Dated: 6 August 2021)

In this paper a methodology is presented to compute the plasma properties (e.g. density and temperature) accounting for the dynamics of the excited states. The proposed strategy applies to both 0-dimensional (0D) models and multidimensional fluid and hybrid codes handling low-pressure (< 50 mTorr) plasma discharges filled with argon, neon, krypton and xenon gases. The paper focuses on two main aspects: (i) a lumping methodology is proposed to reduce the number of reactions and species considered in order to keep at bay the computational cost without a major loss of accuracy; (ii) the influence that different datasets of cross-sections have on the results has been assessed. First the lumping methodology has been implemented in a 0D model accounting for singly-charged ions, neutrals, along with $1s$ and $2p$ excited states (Paschen notation). Metastable and resonant are treated as two separate species within the $1s$ energy level ($1s_M$ and $1s_R$ respectively). Results have been benchmarked against those obtained treating each energy level of the excited states as an individual species. Differences lower than 1% have been obtained. Second, the results of the 0D model have been compared against measurements of electron density and temperature performed on an Inductively Coupled Plasma (ICP). Numerical predictions and experiments present a disagreement up to 20%-30% which is comparable to the uncertainty band of the measurements. Finally, the lumping strategy has been implemented in a 2D fluid code to assess its computational affordability and results have been compared against experiments as well. A variance up to 30% in electron density and temperature is registered adopting different datasets of cross-sections.

I. INTRODUCTION

A deep interest in the development of plasma discharges for industrial^{1,2} and space propulsion applications³⁻⁷ has been growing since the past decades. The research on plasma sources has been particularly active in the fields of electric space propulsion⁸⁻¹⁰, radar and telecommunications¹¹⁻¹⁴, etching of semiconductors², along with lightning technology¹⁵. A notable niche is within the space segment where consolidated plasma-based technologies (e.g., gridded ion and Hall-effect thrusters¹⁶) and novel propulsion concepts are available in the market. Amongst the latter, promising devices are the Radio Frequency (RF) plasma thrusters (e.g., Helicon Plasma Thrusters^{4,8,9,17,18} and the Variable Specific Impulse Magnetoplasma Rockets⁶), the Electron Cyclotron Resonance (ECR) thrusters¹⁹, and the magnetoplasma dynamic thrusters²⁰. Being particularly simple to store and to handle, noble gases like argon, neon, krypton and xenon are frequently used for plasma production. In particular, argon is one of the most used gases in industrial and laboratory discharges², neon is common in lightning technology²¹, along with krypton and xenon are widely used in space propulsion thanks to their good propulsive performance^{16,22,23}.

The increasingly maturity of plasma technologies has brought to the need for more accurate and reliable numerical simulations of the discharges. In this regard, the mod-

elling of the excited states and their fine-structure plays a non-negligible role^{2,24}. In literature, several approaches have been pursued to simulate plasma discharges accounting for the dynamics of the excited states. Collisional-Radiative Models (CRM) are numerical tools that describe very carefully the transitions between different excited states. Several CRMs for argon plasma have been developed, for instance Boegarts²⁵ considered 65 energy levels for studying a 1 kV glow discharge. Vlcek, developed a CRM²⁶ based on the atomic corrected model of Katsonis²⁷ and applied it to atmospheric arcs²⁸, low pressure (< 50 mTorr) glow discharges and hollow cathodes²⁹. In the latter case he considered transitions only between $1s$ and $2p$ states (in Paschen notation). A similar approach is found in the work of Zhu³⁰ for the low pressure cases for which transitions between $1s$ and $2p$ were considered. Regarding neon, Navratil²¹ developed a CRM for studying low pressure positive columns; the interactions between $1s$, $2p$ and higher states have been considered. A similar approach has been adopted by Baghel³¹. Regarding krypton, Gangwar developed a CRM³² for discharges where the pressure ranges between 1-50 mTorr and considered the dynamics of $1s$, $2p$ and few higher states. Prince performed a similar study for krypton-fed Hall Effect Thrusters²³, whereas Priti³³ and Zhu³⁴ did it for xenon. A broader review on CRMs can be found in Van Sijde³⁵. The main drawback of CRMs is that they provide a 0-Dimensional (0D) description of the system. The profiles of the plasma parameters (e.g., density and temperature) are assumed constant or prescribed by heuristic expressions², not derived by the solution of conservation equations. A different approach to simulate the plasma dynamics relies on multidimensional fluid or hybrid solvers^{36,37}. In 1D, 2D and 3D models plasma profiles are solved (and not assumed) even though the dynamics of the excited species is

^{a)}Corresponding author: nabil.souhair2@unibo.it

^{b)}Electronic mail: mirko.magarotto@unipd.it

^{c)}Electronic mail: enrico.majorana@studio.unibo.it

^{d)}Electronic mail: fabrizio.ponti@unibo.it

^{e)}Electronic mail: daniele.pavarin@unipd.it

treated with a much lower accuracy with respect to CRMs to avoid an excessive computational burden. In several fluid and hybrid codes the dynamics of the excited species have been neglected^{38–40}, in other cases only neutral and charged particles have been tracked⁴¹. In this regard, many authors assumed that the excited states decay immediately and thus they modeled them just as a loss term in the electron energy equation. Some solvers adopted this strategy for simulating argon^{42,43} and xenon^{38,39,44,45} discharges. Other authors consider the excited states by lumping them into one or few effective species. This approach has been used both for argon^{46–48} and krypton⁴⁹ discharges. Meunier⁵⁰ used a similar strategy for neon, but no details on the lumping methodology has been provided. According to the scope of this paper, only a limited number of fluid and hybrid solvers have been referenced; a more complete review can be found in Kim³⁷ or in Van Dijk³⁶.

The modelling of the excited states is further complicated by the variance between the cross-sections proposed by different authors. In this regard, Pitchford⁵¹ performed a comparative analysis of electron-neutral scattering cross-sections for argon. Swarm parameters like excitation and ionization coefficients from the cross-sections have been computed and compared against measured values. An analogue analysis was done for krypton and xenon by Bordage⁵² and for neon by Alves⁵³. Nonetheless, to the best of the authors knowledge, a comparative study to assess how such variance affects the prediction of plasma parameters, like electron density, has never been published in literature.

In this work we analyse the influence that the excited states have on the numerical predictions of plasma properties as density and temperature (i.e., not for spectroscopic purposes). In this regard, the analysis covers two main aspects: (i) definition of a lumping methodology to reduce the energy levels considered, (ii) evaluation of the effect that different datasets of cross-sections have on the numerical results. **The lumping strategy aims at the accurate simulation of the excited species with a reduced computational cost and with easier algorithms since only a limited number of species is solved. These features are paramount when the simulation of a plasma discharge shall be iterated numerous times (e.g., for the sensitivity analysis on cross-sections performed in this work) or when dealing with multidimensional codes.** The target application of this paper is low-pressure discharges (< 50 mTorr) filled with argon, neon, krypton and xenon gases. First, the lumping methodology has been implemented in a 0D model. Results have been benchmarked against those obtained treating each energy level of the excited states as an individual species (i.e., the approach implemented in CRMs). Second, for each gas considered, the estimated plasma density and electron temperature have been validated against the measurements performed on an Inductively Coupled Plasma (ICP)⁵⁴. Different datasets of cross-sections have been used in order to assess their influence on the results and, in turn, on the agreement between experiments and simulations. Third, the lumping methodology has been implemented in a 2D fluid code^{46,47,55} that handles a magnetized plasma in order to assess its computational affordability. The results of the fluid code have been compared against measurements performed on a Piglet reac-

tor⁵⁶. Finally, the reaction rate coefficients resulting from the combination of datasets have been analytically fitted for each gas and explicitly presented in the appendix.

II. METHODOLOGY

In argon, neon, krypton and xenon discharges the species considered are electrons, singly-charged ions, neutrals, and excited states within the fine-structure of the $1s$ and $2p$ energy levels (Paschen notation). In low pressure discharges these species present the highest number-density³⁰. The effect of higher excitation energy levels has been neglected, and the idea behind this assumption is discussed more thoroughly when the comparison between numerical and experimental data is presented. Four sets of reactions have been considered, namely electron ionization, electron excitation/de-excitation, elastic scattering and radiative spontaneous emission^{24,33,57,58}. Since a low pressure regime is considered, Penning and heavy species reactions are not treated³⁰. It is worth noting that the same transitions have been considered for argon, neon, krypton and xenon provided they are noble gases which share the same electronic configuration of the outermost shell⁵⁹.

In Sec. II A the excited states and their transitions are discussed. The general lumping methodology is described in Sec. II B. In Sec. II C and Sec. II D the numerical models used, respectively a *Global Model* and a 2D fluid solver^{46,55}, are outlined. The two tools are particularized to RF plasma sources (namely, ICP⁵⁴ and Piglet reactor⁶⁰) even though the lumping procedure can be applied to a generic low pressure discharge.

A. Modelling of the excited states

Regarding the $1s$ excited state, both resonant (i.e., $1s_4$ and $1s_2$) and metastable (i.e., $1s_5$ and $1s_3$) energy levels are taken into consideration. It is worth specifying that the metastable energy levels are those that do not decay via radiative spontaneous emission. Regarding the $2p$ species, all ten levels of the group are considered. In Tab. I, the excited states and the related energy potentials are summarized for argon, neon, krypton and xenon. The species involved and their transitions are schematically described in Fig. 1. It is worth pointing out that the transitions among the excited states of the same type (e.g., $2p$) have been neglected while collisional reactions between metastable ($1s_5$ and $1s_3$) and resonant ($1s_4$ and $1s_2$) species have been considered.

For each electron reaction considered (i.e., electron excitation, electron ionization and elastic scattering), the rate coefficients are computed as:

$$K_{ij} = \sqrt{\frac{2q}{m}} \int_0^\infty \epsilon \sigma_{ij} f_0 d\epsilon \quad (1)$$

where i, j represent respectively the starting lower level and the arriving higher energy level, q and m are the elementary

TABLE I. Argon, neon, krypton, xenon energy states in Paschen notation with related energy levels and statistical weights⁵⁹.

Level	Paschen config.	Excited states				g_i
		Ar U_i [eV]	Ne U_i [eV]	Kr U_i [eV]	Xe U_i [eV]	
1	gs	0	0	0	0	1
2	1s ₅	11.55	16.62	9.92	8.32	5
3	1s ₄	11.62	16.67	10.03	8.44	3
4	1s ₃	11.72	16.72	10.56	9.45	1
5	1s ₂	11.83	16.85	10.64	9.57	3
6	2p ₁₀	12.91	18.4	11.30	9.58	3
7	2p ₉	13.08	18.56	11.44	9.69	5
8	2p ₈	13.09	18.58	11.45	9.72	7
9	2p ₇	13.15	18.61	11.53	9.79	3
10	2p ₆	13.17	18.64	11.55	9.82	5
11	2p ₅	13.27	18.69	11.67	9.93	1
12	2p ₄	13.28	18.70	12.1	10.96	3
13	2p ₃	13.30	18.71	12.14	11.05	5
14	2p ₂	13.33	18.73	12.14	11.07	3
15	2p ₁	13.48	18.97	12.26	11.14	1
16	ion	15.76	21.56	14.00	12.13	

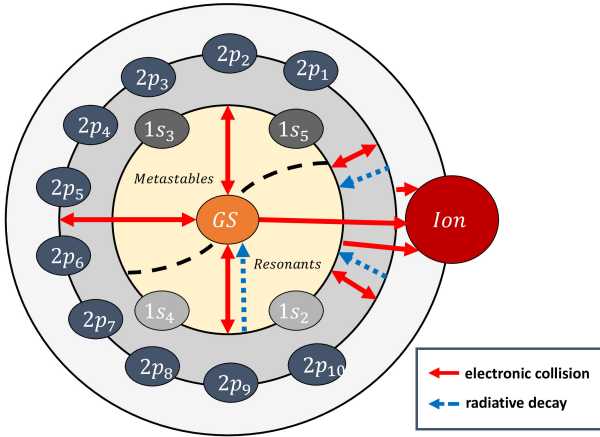


FIG. 1. Species and transitions considered in this work: the solid arrows represent the excitation/de-excitation and ionization transitions by means of electron collisions, the dashed arrows indicate the radiative transitions, and the dashed lines describe the population exchange between metastable and resonant 1s species.

charge and the electron mass; σ_{ij} is the electron-impact cross-section for the transition from the lower state i to the upper state j , ε is the electron energy expressed in eV, and f_0 is the electron energy distribution function (EEDF). In the following, a Maxwellian EEDF has been assumed; in case more accurate experimental measurements of the EEDF are available⁶¹, they can be easily inserted in Eq. (1). The analytical expression of the Maxwellian EEDF reads⁶²,

$$f_0(\varepsilon) = 2\sqrt{\left(\frac{1}{T_e^3\pi}\right)} \exp\left(-\frac{\varepsilon}{T_e}\right) \quad (2)$$

To compute the rate coefficients for the reverse transitions (i.e., electron de-excitation), the *principle of detailed balance*

(DBP) was assumed. The required cross-sections read²

$$\sigma_{ji}(\varepsilon - \Delta U_{ij}) = \frac{g_i}{g_j} \frac{\varepsilon}{\varepsilon - \Delta U_{ij}} \sigma_{ij}(\varepsilon) \quad (3)$$

where σ_{ji} represents the inverse cross-section, $\Delta U_{ij} = U_j - U_i$ is the energy difference between the two states, along with g_i and g_j are the statistical weights which represent the degeneracy of respectively the lower and the higher energy level. The inverse cross-section is then introduced in Eq. (1) to obtain the rate coefficient.

Regarding the radiative transitions only spontaneous emission is taken into consideration. The radiative spontaneous emission is associated to a resonant species at the energy level j that decays towards a lower level i with a rate proportional to the *Einstein* coefficient A_{ji} . In particular, a correction factor Λ_{ji} called *escape factor*, is adopted to account for the self-absorption of the radiation by the plasma. The model proposed by Mewe⁶³ has been adopted. Under the hypothesis of uniform distribution of emitting and absorbing particles, Λ_{ji} reads

$$\Lambda_{ji} = \frac{2 - e^{-\rho\beta_{ji}/1000}}{1 + \rho\beta_{ji}} \quad (4)$$

where ρ is the characteristic length of the geometric domain, and β_{ji} is the reabsorption coefficient for the transition $j \rightarrow i$. Since low temperature plasma is considered (i.e., $T_e < 20$ eV), the Doppler broadening is the main significant mechanism of reabsorption⁵⁷, hence β_{ji} reads

$$\beta_{ji} = \frac{g_j}{g_i} \frac{\lambda_{ji}^3}{8\pi^{3/2}} n_i A_{ji} \sqrt{\frac{M}{2k_B T_0}} \quad (5)$$

where λ_{ji} is the wavelength corresponding to the optical transition $j \rightarrow i$, n_i is the number density of the i -th excited state, M is the particle mass, k_B is the Boltzmann constant, and T_0 is the gas temperature (expressed in Kelvin).

Statistical weights, energy levels, and Einstein coefficients are taken from the *National Institute of Standard and Technology* (NIST) database⁵⁹. The cross-sections for the collisional transitions considered are discussed in Sec. III.

B. Lumping of the energy levels

Following the dynamics of all the excited species (namely, accounting for the fine structure) involves a large number of balance equations to be solved, which leads to an unmanageable computational requirement when fluid (or hybrid) strategies are considered for simulating a plasma discharge. Thus, in order to reduce the number of equations to solve, a lumping procedure based on the assumption of Local Thermodynamic Equilibrium (LTE)⁶⁴ has been introduced. The LTE hypothesis is not in general verified in low pressure discharges^{35,64} but, according to McWhirter's formula⁶⁴, species whose energy is within a certain energy range can be considered in LTE whenever

$$n_e > 10^{19} T_e^{0.5} (\Delta U)^3 \quad (6)$$

where n_e is the electron density, T_e the electron temperature and ΔU the energy gap between different excited levels. For a low temperature plasma (say below 20 eV) this condition is satisfied for $n_e > 10^{16} \text{ m}^{-3}$ for the fine energy levels of both the $1s$ and $2p$ excited states.

Considering an electronic collision transition from a lumped level I to an higher level J



the population density increment in time for the lumped states J reads

$$\frac{dn_J}{dt} = K_{IJ} n_I n_e = \sum_i^{N_i} \sum_j^{N_j} K_{ij} n_i n_e \quad (8)$$

$i = 1, \dots, N_i; \quad j = 1, \dots, N_j$

where n_I and n_J are the number densities of the lumped states I and J , i and j span the fine-structure of the lumped states that group respectively N_i and N_j electronic energy levels, K_{IJ} is the lumped rate coefficient, and K_{ij} accounts for transitions at fine-structure level. In particular K_{IJ} reads

$$K_{IJ} = \frac{\sum_i^{N_i} \sum_j^{N_j} K_{ij} n_i}{\sum_k^{N_I} n_k} \quad (9)$$

Since we consider that LTE holds between the fine-structure energy levels of a lumped state, the Boltzmann relation holds true, namely

$$\frac{n_k}{n_i} = \frac{g_k}{g_i} \exp\left(-\frac{U_k - U_i}{k_B T_0}\right) \quad (10)$$

where the indices k and i refer to generic levels of the fine-structure. Rearranging Eq. (9) in terms of Eq. (10), K_{IJ} reads

$$K_{IJ} = \sum_i^{N_i} \left[\frac{\sum_j^{N_j} K_{ij}}{\sum_k^{N_i} \frac{g_k}{g_i} \exp\left(-\frac{U_k - U_i}{k_B T_0}\right)} \right] \quad (11)$$

TABLE II. Species considered; the excited species are grouped in lumped states.

Lumped species	Detailed states
gs	ground state
$1s_M$	$1s_5, 1s_3$ (metastable)
$1s_R$	$1s_4, 1s_2$ (resonant)
$2p$	$2p_{10}, 2p_9, 2p_8, 2p_7, 2p_6, 2p_5, 2p_4, 2p_3, 2p_2, 2p_1$
ion	1^{st} ionization
e	electron

The lumped rate coefficient for the inverse transition K_{JI} is obtained combining Eq. (9), Eq. (10) and the DBP; it reads

$$K_{JI} = \sum_j^{N_j} \left[\frac{\sum_i^{N_i} K_{ij} g_i \exp\left(-\frac{U_i}{k_B T_0}\right)}{\sum_k^{N_j} g_k \exp\left(-\frac{U_k}{k_B T_0}\right)} \right] \quad (12)$$

Moreover, the energy potential associated to the lumped states I reads

$$U_I = \frac{\sum_i^{N_i} g_i U_i}{\sum_i^{N_i} g_i} \quad (13)$$

and the lumped statistical weight

$$g_I = \sum_i^{N_i} g_i \quad (14)$$

Regarding the radiative transitions

$$X_J \rightarrow X_I + h\nu \quad (15)$$

the decay rates have been lumped, similarly to Eq.9, as

$$A_{JI} \Lambda_{JI} = \frac{\sum_i^{N_i} \sum_j^{N_j} n_j A_{ji} \Lambda_{ji}}{\sum_k^{N_j} n_k} \quad (16)$$

The excited species have been grouped into three lumped levels, namely $1s_M$, $1s_R$, $2p$. The species considered are listed in Tab. II, while lumped reactions in Tab. III. Finally, it is worth noting that, technically, the lumping methodology has not been applied to the electron impact ionization reactions since the cross-sections found in literature concerns the lumped states $1s$ and $2p$, not their fine structure.

C. Global Model

A 0D *Global Model*^{2,65} has been adopted to evaluate the plasma properties in an ICP discharge⁵⁴. The governing equations encompass mass and energy conservation

$$\frac{dn_I}{dt} = R_{chem}^I - R_{wall}^I \quad (17a)$$

$$\frac{d}{dt} \left(\frac{3}{2} n_e T_e \right) = P - P_{chem} - P_{wall} \quad (17b)$$

TABLE III. Reactions that involve lumped excited states.

Reactions	Reaction type
$gs + e \rightleftharpoons 1s_M + e$	Excitation / de-excitation
$gs + e \rightleftharpoons 1s_R + e$	Excitation / de-excitation
$gs + e \rightleftharpoons 2p + e$	Excitation / de-excitation
$1s_M + e \rightleftharpoons 1s_R + e$	Excitation / de-excitation
$1s_M + e \rightleftharpoons 2p + e$	Excitation / de-excitation
$1s_R + e \rightleftharpoons 2p + e$	Excitation / de-excitation
$gs + e \rightarrow gs + e$	Elastic scattering
$1s_M + e \rightarrow 1s_M + e$	Elastic scattering
$1s_R + e \rightarrow 1s_R + e$	Elastic scattering
$2p + e \rightarrow 2p + e$	Elastic scattering
$gs + e \rightarrow ion + e$	Electron impact ionization
$1s_M + e \rightarrow ion + e$	Electron impact ionization
$1s_R + e \rightarrow ion + e$	Electron impact ionization
$2p + e \rightarrow ion + e$	Electron impact ionization
$1s_R \rightarrow gs + h\nu$	Decay towards lower state
$2p \rightarrow 1s_M + h\nu$	Decay towards lower state
$2p \rightarrow 1s_R + h\nu$	Decay towards lower state

where n_I is the number density of the I -th species (with $I = gs, 1s_M, 1s_R, 2p, ion$, and e), and T_e is the electron temperature. Specifically, n_I represent bulk quantities, instead T_e is a volume-averaged value. The temperature of ions, neutrals and excited states (T_0) is assumed and not computed⁴⁶. R_{chem}^I is the term associated to the production/loss of I -th type particles due to the reactions, and it reads

$$R_{chem}^I = \sum_J K_{JI} n_J n_e - \sum_J K_{IJ} n_I n_e + \sum_{J>I} A_{JI} \Lambda_{JI} n_J - \sum_{J<I} A_{IJ} \Lambda_{IJ} n_I \quad (18)$$

R_{wall}^I is the term associated to the loss/production of I -th type particles due to the interaction with the walls. It reads,

$$R_{wall}^I = \frac{S^I}{V} \Gamma_{wall}^I \quad (19)$$

where S^I is the equivalent surface of the discharge for the I -th species², V is the volume of the discharge, and Γ_{wall}^I is the flux of particles toward the wall. For ions and electrons $S^e = S^i$ is computed according to the empirical relations reported in Lieberman², and $\Gamma_{wall}^e = \Gamma_{wall}^i = n_e \sqrt{qT_e/M}$ according to the sheath model proposed by Ahedo⁶⁶ which basically enforces the Bohm criterion^{67,68}. For excited species, S^I is equal to the physical surface of the discharge, and $\Gamma_{wall}^I = 1/4 n_I v_{th}$ where $v_{th} = \sqrt{8k_B T_0 / \pi M}$ ⁴⁶. Assuming that charged and excited particles recombine at the wall, $R_{wall}^{gs} = -\sum_I R_{wall}^I$. P is the electrical power deposited within the discharge by the antenna. P_{chem} is the power loss/source term associated to reactions, which reads²

$$P_{chem} = \sum_I \sum_J K_{IJ} n_I n_e \Delta U_{IJ} + \sum_I K_{II} n_I n_e \frac{3m}{M} T_e \quad (20)$$

where K_{II} is the rate coefficient for the elastic scattering, and m is the electron mass. Finally, P_{wall} represents the energy loss to the walls and, according to the sheath model described in Ahedo⁶⁶, it reads

$$P_{wall} = R_{wall}^e \left(2T_e \frac{1}{1-\gamma} - 2T_s \frac{\gamma}{1-\gamma} + \phi_{wall} \right) \quad (21)$$

where γ is the fraction of secondary electrons emitted by the wall, T_s is the temperature of the secondary electrons and ϕ_W is the potential drop through the sheath. The latter parameter reads

$$\phi_{wall} = T_e \log \left(\sqrt{\frac{M}{2\pi m}} (1-\delta)(1-\gamma) \right) \quad (22)$$

where δ is the fraction of electrons elastically reflected by the wall. According to Barral⁶⁹, $\delta = \delta_0 E_r^2 / (T_e + E_r)^2$ and $\gamma = 2T_e / E_s$. The following values have been assumed in the rest of the manuscript $T_s = 2$ eV, $\delta_0 = 0.4$, $E_r = 20$ eV, $E_s = 50$ eV^{69,70}. For further details on the *Global Model* (e.g., definition of the equivalent surface and applicability ranges) refer to Lieberman² and Bosi^{65,71}.

D. Fluid Model

The 3D-VIRTUS code^{46,72} has been used to solve the plasma dynamics in a magnetized Piglet reactor⁶⁰. 3D-VIRTUS handles self-consistently both the plasma transport within the source and the power deposition via the damping of the EM waves. The former is solved in a 2D-axisymmetric domain with a fluid approach. In order to track the dynamics of the excited lumped species, the fluid module of 3D-VIRTUS has been updated; governing equations are outlined in the following. For further details on the code and the underlying hypotheses, the reader is referred to Magarotto⁴⁶. Continuity, energy and Poisson equations read

$$\frac{\partial n_I}{\partial t} + \nabla \cdot \Gamma_I = R_{chem}^I \quad (23a)$$

$$\frac{\partial n_e}{\partial t} + \nabla \cdot \Gamma_e - \nabla \phi \cdot \Gamma_e = P - P_{chem} \quad (23b)$$

$$\nabla^2 \phi = -q \left(\frac{n_{ion} - n_e}{\epsilon_0} \right) \quad (23c)$$

where $n_e = 3/2 n_e T_e$ is the energy density, ϕ is the electrostatic potential arising from charge unbalance, and ϵ_0 is the vacuum permittivity. The terms R_{chem}^I and P_{chem} represent the particle and the energy production/loss due to chemical reactions. Their expression are formally the same reported in Eq. 18 and Eq. 20 respectively with the substantial difference that in 3D-VIRTUS R_{chem} and P_{chem} are scalar fields dependent of space. P is the power deposition profile computed via the EM-module of 3D-VIRTUS⁴⁶. Γ_I is the I -th particles flux and reads, according to the drift-diffusion approximation⁴⁶,

$$\Gamma_I = \mp \tilde{\mu}_I n_I \nabla \phi - \tilde{D}_I \nabla n_I \quad (24)$$

where \bar{D}_I is the diffusivity, and $\bar{\mu}_I$ the mobility. The latter is non-zero for charged species only, and it has positive (negative) values for electrons (ions). For the electrons, \bar{D}_e and $\bar{\mu}_e$ have a dyadic expression to account for magnetization⁴⁶. Γ_ϵ is the energy flux and, according to the drift-diffusion approximation, it reads

$$\Gamma_\epsilon = \bar{\mu}_\epsilon n_\epsilon \nabla \phi - \bar{D}_\epsilon \nabla n_\epsilon \quad (25)$$

Electron mobility in absence of magnetic field is a scalar variable dependent of space that reads $\mu_e = q/m \sum_I \sum_J K_{IJ} n_I$; starting from this value, $\bar{\mu}_e$ can be computed as prescribed in the work of Souhair⁵⁵. According to Einstein relations, $\bar{D}_e = \bar{\mu}_e T_e$, $\bar{\mu}_\epsilon = 5/3 \bar{\mu}_e$, and $\bar{D}_\epsilon = \bar{\mu}_\epsilon T_e$. Finally, diffusivity and mobility for ions, neutrals, and excited species are computed as prescribed in Magarotto⁴⁶.

A Robin boundary condition is imposed to the continuity of the electrons and the energy in order to enforce the sheath model proposed by Ahedo that accounts for the secondary emission and the elastic reflection at the walls^{46,66}. A Robin condition is imposed to the continuity of the ions^{46,73}. A Neumann condition on the continuity of neutrals and excited species enforces thermal diffusion and wall recombination⁴⁶. Finally, a Neumann condition is imposed to the Poisson equation so that ion and electron fluxes are equal at the walls⁴⁵

$$\frac{\partial \phi}{\partial x_\perp} = \frac{1}{\mu_i n_i} \left(-\Gamma_{wall}^e + \frac{1}{2} v_{th} n_i \right) \quad (26)$$

In Eq. (26), x_\perp is the direction perpendicular to the boundary and Γ_{wall}^e has been defined in Sec. II C.

III. RESULTS

A. Global Model

The ICP reactor characterized by Schwabedissen¹⁵ provides a realistic numerical setup to: (i) benchmark the lumping methodology against a detailed analysis of the fine-structure energy levels of the excited species as done in CRMs, (ii) validate the lumping methodology against experiments, (iii) quantify the influence that the cross-section datasets have on the results. The *Global Model* described in Sec. II C has been used to simulate the ICP when operated with argon, neon, krypton and xenon gases. The species tracked are electrons, singly-charged ions, neutrals at ground state, and excited (i.e., $1s_M$, $1s_R$, and $2p$ lumped energy levels). Moreover, a preliminary analysis has been accomplished to identify the transitions between excited levels that mainly affect the numerical results. To this end, three different cases have been simulated: (i) purely collisional case in which radiative transitions have been neglected; (ii) collisional case with the addition of the $1s$ radiative decay, (iii) collisional-radiative case where all the transitions involving both $1s$ and $2p$ have been accounted for. **The latter case, which gives the more complete description of the plasma dynamics, has been used to benchmark and validate the lumping methodology.** It

TABLE IV. Input parameters of the Global Model used to simulate the ICP reactor.

Parameter	Value
Diameter	165 mm
Length	40.5 mm
Magneto-static field	0 T
Gas pressure	20 mTorr

is worth highlighting that the variance of the plasma parameters obtained combining different cross-sections depends on the choice of the datasets. The one used in this work include, but are not limited to, the datasets mentioned in the seminal reviews by Pitchford⁵¹, Bordage⁵² and Alves⁵³ which cover a significant portion of the literature.

The Schwabedissen's setup consists in an ICP reactor derived from the GEC RF Reference Cell proposed by Miller⁵⁴. Accordingly to the description reported in^{15,54}: (i) the setup comprises a cylinder discharge chamber with inner diameter 165 mm and length 40.5 mm, (ii) there is no applied magneto-static field, (iii) the gas pressure at standard ambient temperature, namely before plasma ignition, is equal to 20 mTorr. The antenna is realized with five turn spiral coils of outer diameter 100 mm made of 3 mm copper tubing. The antenna is powered at a frequency of 13.56 MHz through a matching network made of two air-dielectric variable capacitors⁵⁴. A Langmuir probe realized with a tungsten wire of radius 75 μm has been used to characterize the source in terms of plasma density and temperature. The measurements considered in this work are taken along the discharge axis, 12 mm above the lower base of the cylindrical chamber. The source has been tested for different values of the deposited power (i.e., power coupled to the plasma) which has been estimated comparing the impedance of the system at plasma off and plasma on¹⁵. The gases considered are argon, neon, krypton and xenon. The input parameters used in the *Global Model* are synthetically summarized in Tab. IV.

1. Benchmark of the lumping strategy

A benchmark case is presented in order to demonstrate the correctness and robustness of the lumping methodology^{74–76}. To this end, the plasma properties (density and temperature) predicted through the lumping methodology have been compared against the ones obtained treating each fine-structure energy level of the excited states as an individual species⁷⁷ (see Tab. I). The Schwabedissen's ICP reactor operated with argon gas was simulated with the *Global Model* presented in Sec. II C. The two approaches differ mainly for the number of species treated and for the formulation of Eqs. (17–22), namely for what the mass and power generation/loss terms are concerned. According to the lumping methodology, Eqs. (17–22) are computed for the set of reactions shown in Tab. III. Instead each fine-structure transition is considered while solving the dynamics of the excited species with the approach implemented in CRMs³⁰. The rate con-

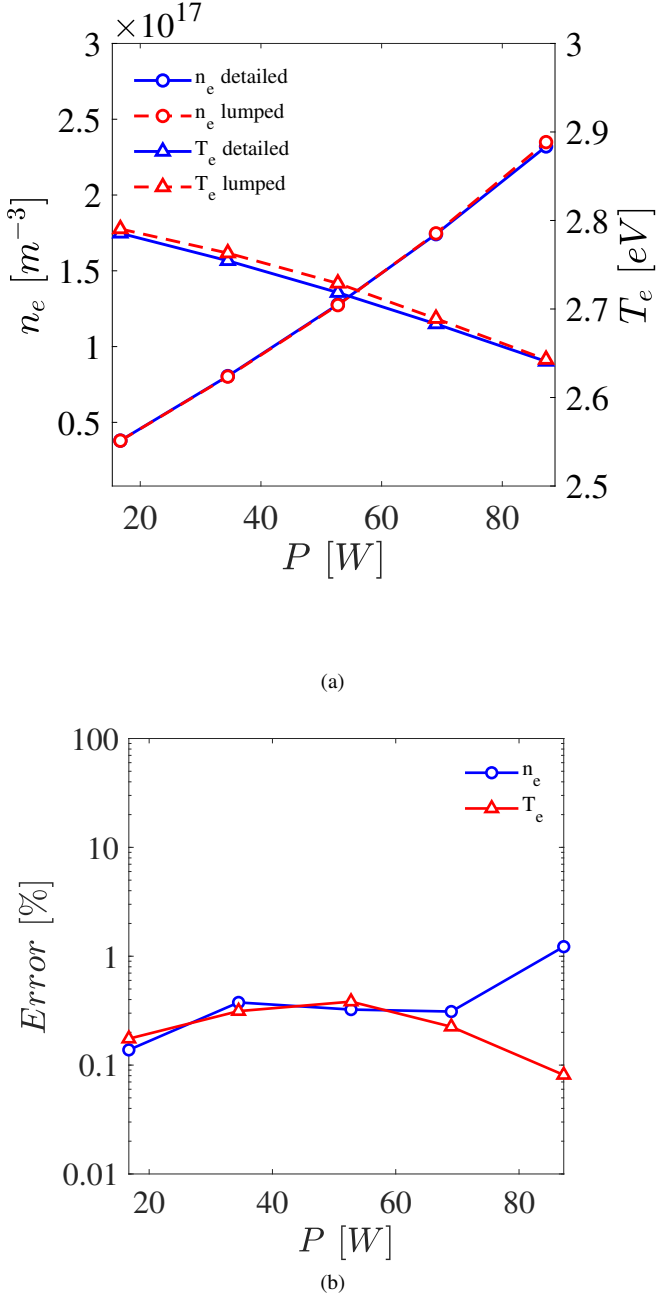


FIG. 2. (a) Electron density (n_e) and electron temperature (T_e) in function of the deposited power (P), data are obtained with the lumping strategy or the detailed simulation of the excited states, (b) percent error between n_e and T_e calculated with the detailed and the lumping methodologies.

stants proposed by Zhu³⁰ have been employed for this analysis. Electron density (n_e) and temperature (T_e) predicted through the lumping or the detailed methodology present the same trends (see Fig. 2a): n_e increases with the deposited power (P) while T_e mildly decreases. In order to quantify

TABLE V. Datasets of argon cross-sections for excitation reactions.

Excitation	Database reference
$gs + e \rightarrow 1s + e$	78–85
$gs + e \rightarrow 2p + e$	78–84,86
$1s + e \rightarrow 1s + e$	82,83,87
$1s + e \rightarrow 2p + e$	82,83,87–89

TABLE VI. Datasets of argon cross-sections for elastic scattering reactions.

Elastic scattering	Database reference
$gs + e \rightarrow gs + e$	78,80–84,90–92
$1s + e \rightarrow 1s + e$	78,80–84,90–92
$2p + e \rightarrow 2p + e$	78,80–84,90–92

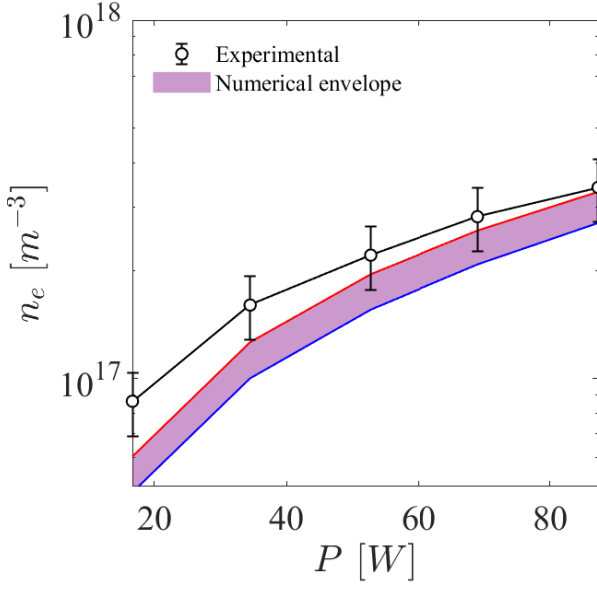
TABLE VII. Datasets of argon cross-sections for ionization reactions.

Ionization	Database reference
$gs + e \rightarrow ion + e$	78–84,90,92–94
$1s + e \rightarrow ion + e$	95,96
$2p + e \rightarrow ion + e$	95,96

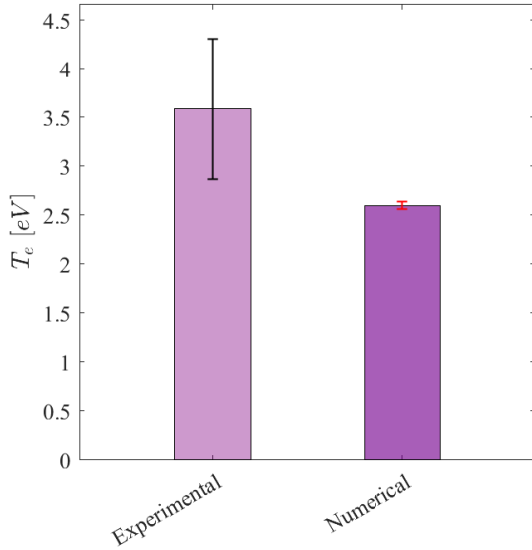
the relative error between the two approaches, the quantity $Error = 2|x_{detailed} - x_{lumped}|/(x_{detailed} + x_{lumped})$ has been depicted in Fig. 2b in function of P . Regardless the value of P , the percent error between steady state values of n_e and T_e is generally below 1%. This proves the reliability and the robustness of the proposed lumping methodology.

2. Argon

In Fig. 3 numerical data are compared against experiments when the ICP reactor is operated with argon gas. The electron density is depicted as a function of the deposited power (see Fig. 3a). Only the average value of the electron temperature is reported (see Fig. 3b) since it is almost independent on the deposited power¹⁵. Measurements have been sampled along the axis of the discharge with a Langmuir probe¹⁵; the uncertainty on both n_e and T_e is in the order of 20%¹⁵. The numerical results have been computed using the cross-section datasets listed in Tab. V-VII. All the possible combinations of cross-sections have been considered. Therefore numerical results are depicted as an envelope of data comprised between two boundary values, namely they are affected by an error



(a)



(b)

FIG. 3. Comparison between numerical and experimental data when the ICP reactor is operated with argon gas. (a) Electron density n_e as a function of the deposited power P (b) average electron temperature T_e . The numerical envelope refers to results obtained with cross-sections from different datasets. Measurements reported with an uncertainty band of $\pm 20\%$.

bar related to the uncertainty on the cross-sections. Numerical

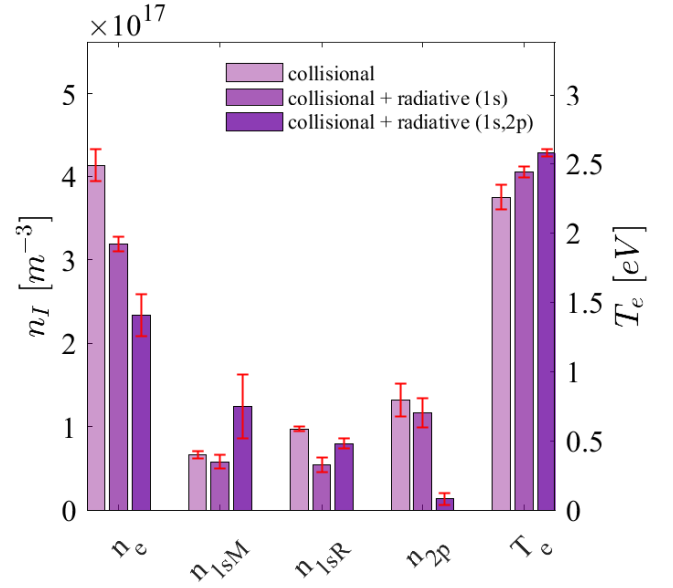


FIG. 4. Argon gas, deposited power $P = 70$ W. Numerical predictions of density n_I ($I = e, 1s_M, 1s_R, 2p$ for the electrons and the excited species respectively) and electron temperature T_e . Error bars associated to the uncertainty on the cross-sections.

cal predictions of n_e underestimate the experimental data by 12%; the numerical error bar is about 20%. The electron temperature is underestimated by 29%. The lowest (highest) values of plasma density correspond to highest (lowest) electron temperatures, the latter differ by 1.5%.

In order to preliminary investigate the role played by transitions between excited species, density of electrons (n_e) and excited species (n_{1s_M} , n_{1s_R} , and n_{2p}), along with electron temperature (T_e) have been reported in Fig. 4. Three cases have been compared: purely collisional, collisional plus 1s radiative decay, and collisional-radiative (i.e., the one used for the validation). For the sake of brevity, results are discussed only for $P = 70$ W. In the collisional-radiative case n_e is about 40% lower with respect to the purely collisional case, instead T_e increases of about 0.3 eV. The 1s radiative decay affects mildly the population of the excited states. Instead the 2p radiative decay causes a drop in n_{2p} of more than one order of magnitude. In the collisional-radiative case n_{2p} is more then one order of magnitude lower with respect to n_e ; instead n_{1s_M} , n_{1s_R} and n_e are of the same order of magnitude.

3. Neon

In Fig. 5, numerical and experimental data are compared when the ICP reactor is operated with neon gas. The elec-

TABLE VIII. Datasets of neon cross-sections for excitation reactions.

Excitation	Database reference
$gs + e \rightarrow 1s + e$	79,80,82–84,92
$gs + e \rightarrow 2p + e$	80,82–84
$1s + e \rightarrow 1s + e$	-
$1s + e \rightarrow 2p + e$	97

TABLE IX. Datasets of neon cross-sections for elastic scattering reactions.

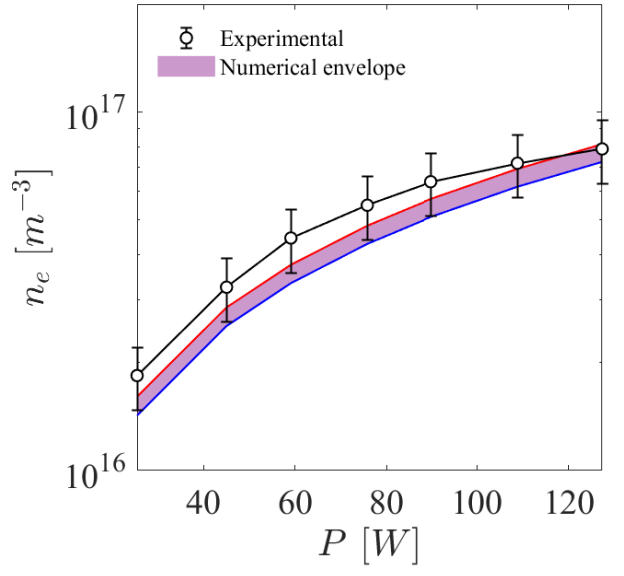
Elastic scattering	Database reference
$gs + e \rightarrow gs + e$	80,82–84,90,92,94
$1s + e \rightarrow 1s + e$	80,82–84,90,92,94
$2p + e \rightarrow 2p + e$	80,82–84,90,92,94

TABLE X. Datasets of neon cross-sections for ionization reactions.

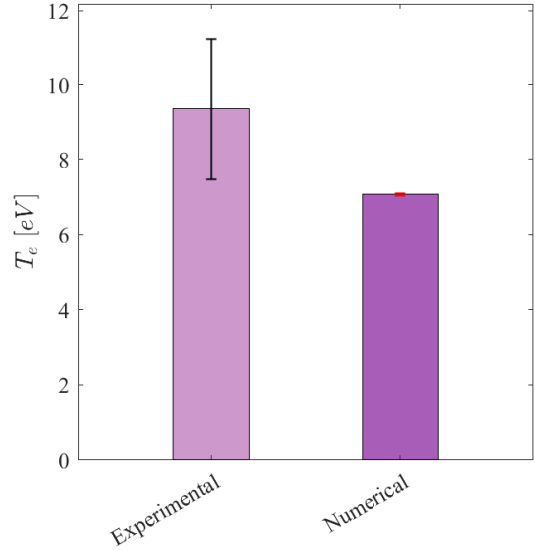
Ionization	Database reference
$gs + e \rightarrow ion + e$	79,80,82–84,90,92–94
$1s + e \rightarrow ion + e$	95
$2p + e \rightarrow ion + e$	95

tron density is depicted as a function of the input power (see Fig. 5a), only the average value of the electron temperature is reported (see Fig. 5b). As in the argon case, the uncertainty on the measures is 20% for both n_e and T_e ¹⁵. Cross-section datasets used for the computation are listed in Tab. VIII-X. The electron density is underestimated by 8% while highest and lowest values differ for about 10%. A disagreement of 2 eV (i.e., a deviation of about 30%) is registered between measures and estimations of the electron temperature. The numerical envelope is quite narrow being the variance of T_e equal to 0.5%.

Results obtained in the collisional, collisional plus $1s$ radiative, and collisional-radiative cases at $P = 110$ W are depicted in Fig. 6. The radiative decay causes a reduction of n_e by 29% with respect to the purely collisional case and an increase of T_e by 1 eV. The $1s$ radiative decay causes a drop of one order of magnitude in n_{1s_R} . This is partly due to having neglected the excitation reaction $1s + e \rightarrow 1s + e$ provided that the authors found no data concerning cross-sections in literature. Likewise, the $2p$ radiative decay causes a drop in n_{2p} of more than one order of magnitude. In the collisional-radiative case n_e and n_{1s_M} are of the same order of magnitude while n_{1s_R} and



(a)



(b)

FIG. 5. Comparison between numerical and experimental data when the ICP reactor is operated with neon gas. (a) Electron density n_e as a function of the deposited power P (b) average electron temperature T_e . The numerical envelope refers to results obtained with cross-sections from different datasets. Measurements reported with an uncertainty band of $\pm 20\%$.

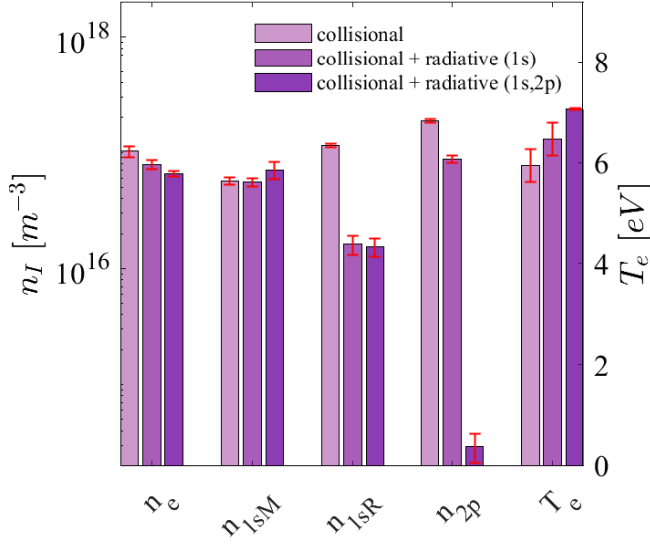


FIG. 6. Neon gas, deposited power $P = 110$ W. Numerical predictions of density n_I ($I = e, 1s_M, 1s_R, 2p$ for the electrons and the excited species respectively) and electron temperature T_e . Error bars associated to the uncertainty on the cross-sections.

TABLE XI. Datasets of krypton cross-sections for excitation reactions.

Excitation	Database reference
$gs + e \rightarrow 1s + e$	82–84,87
$gs + e \rightarrow 2p + e$	82–84,87
$1s + e \rightarrow 1s + e$	87
$1s + e \rightarrow 2p + e$	87

n_{2p} are respectively one and two orders of magnitude smaller.

4. Krypton

The comparison between numerical and experimental data when the ICP reactor is operated with krypton is reported in Fig. 7. The uncertainty on the measure of n_e is 30% due to the impossibility of operating the Langmuir probe for $n_e > 6 \times 10^{17} \text{ m}^{-3}$ to avoid damages¹⁵. At the same time, uncertainty on T_e is 20%¹⁵. Datasets of cross-sections used for the computations are reported in Tab. XI–XIII. A large span in the envelope of n_e can be noticed being experimental values underestimated by 14% or 46% considering highest and lowest density respectively. T_e is underestimated by 26% and the

TABLE XII. Datasets of krypton cross-sections for elastic scattering reactions.

Elastic scattering	Database reference
$gs + e \rightarrow gs + e$	82–84,90–92,94
$1s + e \rightarrow 1s + e$	82–84,90–92,94
$2p + e \rightarrow 2p + e$	82–84,90–92,94

TABLE XIII. Datasets of krypton cross-sections for ionization reactions.

Ionization	Database reference
$gs + e \rightarrow ion + e$	84,90,92,94
$1s + e \rightarrow ion + e$	95
$2p + e \rightarrow ion + e$	95

numerical error bar is about 5%.

Data obtained in the collisional, collisional plus 1s radiative, and collisional-radiative cases for $P = 26$ W are depicted in Fig. 8. The radiative decay causes a reduction in n_e by more than 50% and an increase of T_e by 0.2 eV. As for argon, the 1s radiative decay has a mild influence on the dynamics of the excited species. Instead the 2p radiative decay causes a drop

TABLE XIV. Datasets of xenon cross-sections for excitation reactions.

Excitation	Database reference
$gs + e \rightarrow 1s + e$	80,82–84
$gs + e \rightarrow 2p + e$	82–84
$1s + e \rightarrow 1s + e$	33,98
$1s + e \rightarrow 2p + e$	33

TABLE XV. Datasets of xenon cross-sections for elastic scattering reactions.

Elastic scattering	Database reference
$gs + e \rightleftharpoons gs + e$	80–84,91,92,94
$1s + e \rightleftharpoons 1s + e$	80–84,91,92,94
$2p + e \rightleftharpoons 2p + e$	80–84,91,92,94

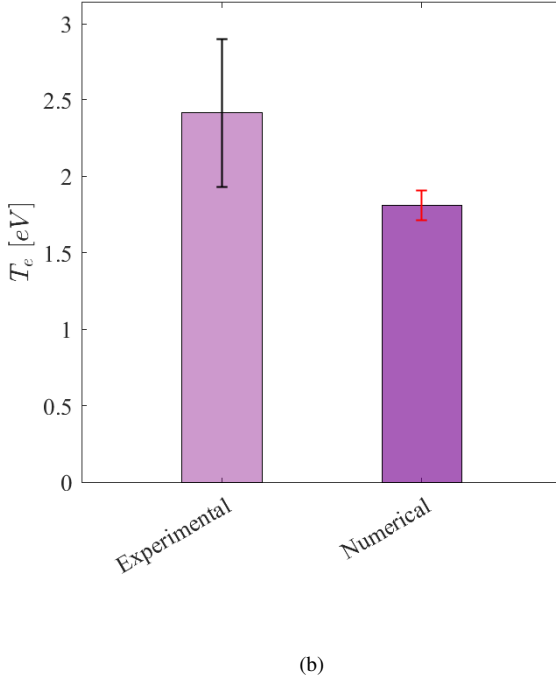
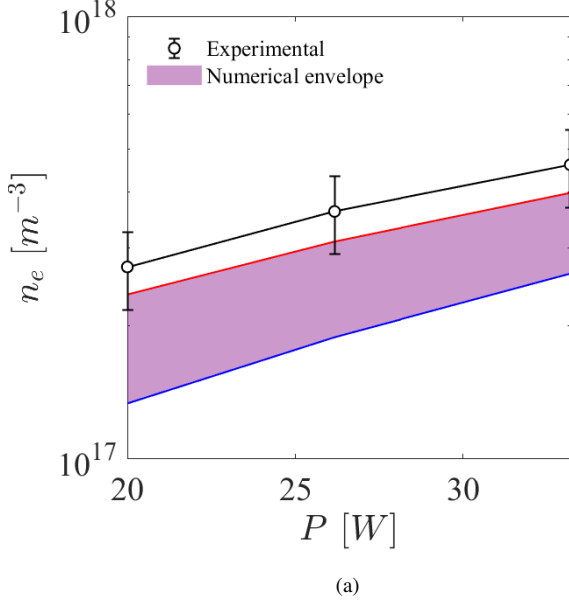


FIG. 7. Comparison between numerical and experimental data when the ICP reactor is operated with krypton gas. (a) Electron density n_e as a function of the deposited power P (b) average electron temperature T_e . The numerical envelope refers to results obtained with cross-sections from different datasets. The uncertainty band is $\pm 30\%$ for n_e measures, $\pm 20\%$ for T_e measures.

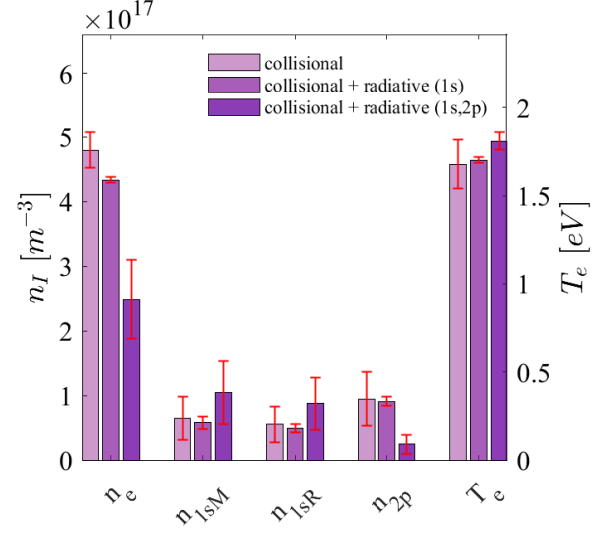


FIG. 8. Krypton gas, deposited power $P = 26$ W. Numerical predictions of density n_I ($I = e, 1s_M, 1s_R, 2p$ for the electrons and the excited species respectively) and electron temperature T_e . Error bars associated to the uncertainty on the cross-sections.

TABLE XVI. Datasets of xenon cross-sections for ionization reactions.

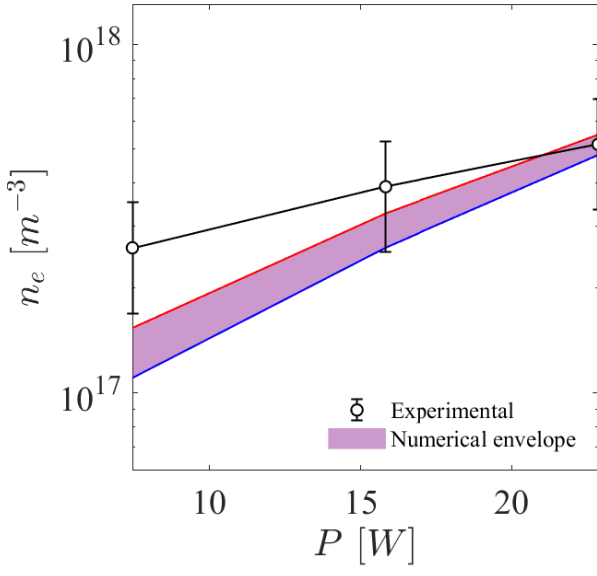
Ionization	Database reference
$gs + e \rightarrow ion + e$	79–81,84,90,92,94
$1s + e \rightarrow ion + e$	95
$2p + e \rightarrow ion + e$	95

in n_{2p} of about one order of magnitude. In the collisional-radiative case n_{2p} is one order of magnitude smaller than n_e , n_{1s_M} and n_{1s_R} .

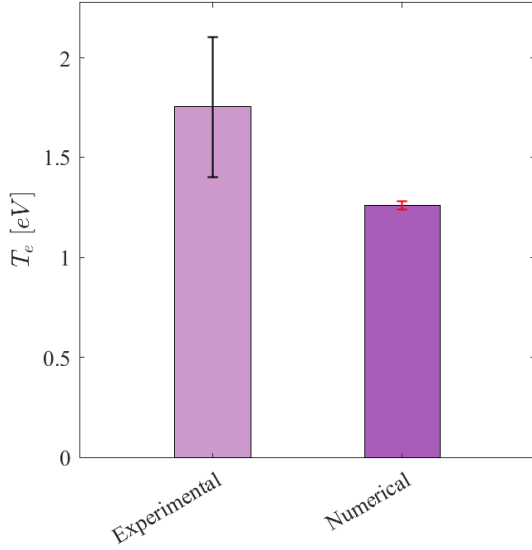
5. Xenon

Results obtained when the working gas is xenon are reported in Fig. 9. As for krypton, the uncertainty on the measures is 30% and 20% for n_e and T_e respectively¹⁵. Datasets of cross-sections used for the computation are reported in Tab. XIV–XVI. Numerical predictions underestimate n_e by 13%; highest and lowest density differ for about 20%. The electron temperature is underestimated by 29% with a variance on T_e of 1%.

Data obtained in the collisional, collisional plus $1s$ radiative, and collisional-radiative cases for $P = 23$ W are depicted in Fig. 10. Xenon is the gas for which the radiative decay causes the highest reduction of n_e , namely more than 60%;



(a)



(b)

FIG. 9. Comparison between numerical and experimental data when the ICP reactor is operated with xenon gas. (a) Electron density n_e as a function of the deposited power P (b) average electron temperature T_e . The numerical envelope refers to results obtained with cross-sections from different datasets. The uncertainty band is $\pm 30\%$ for n_e measures, $\pm 20\%$ for T_e measures.

instead T_e increases by 0.1 eV. The $1s$ radiative decay affects

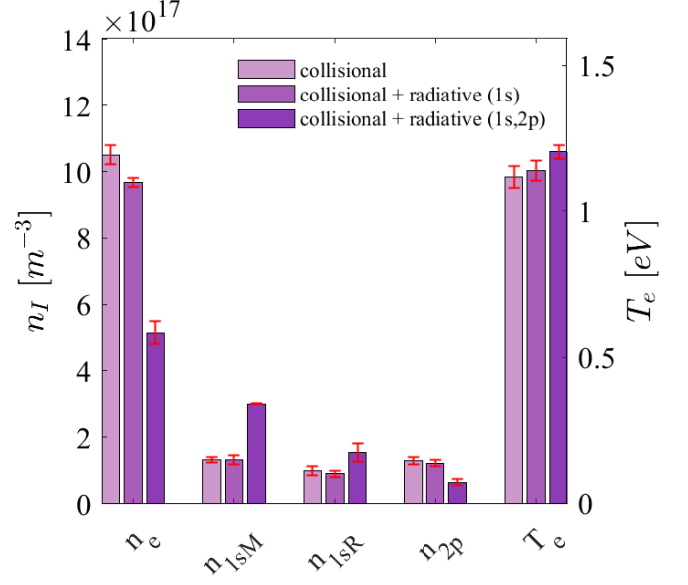


FIG. 10. Xenon gas, deposited power $P = 23$ W. Numerical predictions of density n_I ($I = e, 1s_M, 1s_R, 2p$ for the electrons and the excited species respectively) and electron temperature T_e . Error bars associated to the uncertainty on the cross-sections.

mildly the excited species while the $2p$ radiative decay causes n_{2p} to halve. In the collisional-radiative case n_e , n_{1s_M} , and n_{1s_R} are of the same order of magnitude, while n_{2p} is about one order of magnitude smaller.

6. Discussion

First, the lumping strategy has been benchmarked against the detailed solution in which the dynamics of each fine structure energy levels is tracked. The error between electron density and temperature predicted with the two approaches is generally less than 1%. Second, the results obtained implementing the lumping strategy on the *Global Model* have been validated against experiments. For what electron density is concerned, numerical results are in fairly good agreement with measurements provided that the numerical envelope overlaps the experimental uncertainty band for all the gases. More precisely, the agreement between numerical predictions and experiments is poorer for krypton and xenon with respect to argon and neon. This might be due to two aspects: (i) in larger atoms the energy of the fine structure levels are more spread, so the LTE hypothesis is progressively less robust; (ii) the Langmuir probe adopted by Shwabedissen failed for $n_e > 6 \times 10^{17} \text{ m}^{-3}$ ¹⁵, so the uncertainty of the measures might be higher than 30% getting closer to this limit. Similar considerations hold true for the electron temperature. The difference between numerical and experimental values is be-

tween 19% and 29% in face of a 20% uncertainty band of the measures. Nonetheless, T_e predicted by the *Global Model* is a volume averaged quantity, which is not subject to assumptions on spatial profiles as n_e . This is a possible justification of the mild difference between numerical and experimental estimations of T_e since measures are performed on the axis of the discharge¹⁵. In addition numerical results, both in terms of n_e and T_e , are affected by other assumptions as the sheath model. Expressions for Γ_{wall} and P_{wall} presented in Sec.II.C are quite general provided that secondary electron emission and elastic reflection have been modelled. In addition, the ICP reactors has no electrodes in contact with the plasma and is realized with materials whose behaviour in vacuum is well known (e.g., quartz)^{2,41}. Nonetheless the sheath model is expected to be another moderate source of uncertainty (in the order of 10%^{47,72}). In conclusion, the lumping strategy involving only $1s$ and $2p$ energy levels is proven to predict plasma density and temperature with an uncertainty lower than 30% regardless the gas. This is considered acceptable for a preliminary design tool as the *Global Model* in several applications concerning low pressure plasma discharges^{65,99}.

The choice of the cross-section dataset affects significantly the numerical results. Plasma density presents a variance up to 32% considering krypton gas. Such a large value is not unexpected provided that the R_{chem} and P_{chem} terms (see Eq. 17) depend linearly from the cross-sections. Similar considerations hold true also for the electron temperature, the maximum variance of which, is registered again for krypton (value of 5%). According to the previous results, there is not a set of cross-sections that provide an output closer to experiments in general, namely it is not possible to identify a priori a dataset optimal for each scenario. For this reason, in Appendix A analytical expressions for the rate coefficients adopted in the highest and lowest density cases (i.e., the bounds of the uncertainty band associated to cross-sections) have been reported for each gas.

The analysis performed with the *Global Model* can give some insights into how transitions between excited species affect the dynamics of a plasma discharge. The main effect produced by radiative decay is the reduction of the population of excited species that can be ionized with a lower amount of energy with respect to neutrals. In other words, the radiative decay produces an increase of the P_{chem} term provided that collisional de-excitation and step-wise ionization reactions are less frequent. An increase in the reaction energy losses results in the reduction of the internal energy of the discharge $n_e = \frac{3}{2}n_e T_e$. Regardless the gas type, n_e decreases of 25-35% from the collisional case to the radiative-collisional in response to an increase of P_{chem} of about 20-30%. Consequently, it is not surprising that the radiative decay causes an increase of T_e being the drop of n_e about 30-50% and of n_e only 25-35%. Finally, the population of the excited species has been estimated to be lower with respect to electrons. Depending on the gas, n_{1s_M} and n_{1s_R} are up to one order of magnitude smaller than n_e ; n_{2p} up to two. This is in agreement with previous analyses performed on ICP reactors^{30,100}.

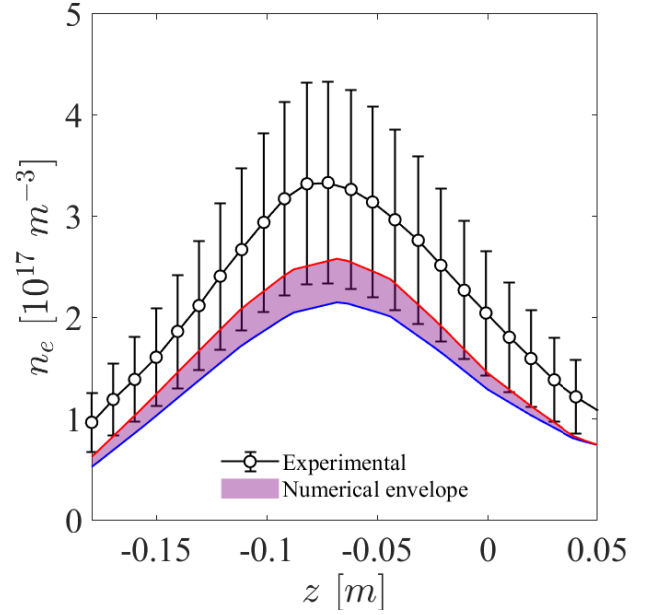


FIG. 11. Electron density n_e as a function of the axial position z within the Piglet reactor. Experimental data are reported with uncertainty band of 25%, the numerical envelope refers to different cross-sections datasets. Results are taken in the centerline of the reactor.

B. Fluid code

The lumping methodology has been implemented in the fluid code discussed in Sec. IID in order to verify its computational affordability. Numerical results have been validated against measurements of the electron density sampled in a magnetized plasma. It is worth highlighting that simulating a magnetized plasma is usually more computational intensive than a non-magnetized one, in fact plasma gradients are steeper so a finer mesh is required⁴⁶. Experimental data, available for argon, are collected along the axis of a Piglet reactor with a Langmuir probe^{46,60}. The cross-section datasets that give the highest and the lowest density in the collisional-radiative case (see Sec. III A 2) have been adopted in order to assess their influence on the plasma density profile, and in turn on the agreement between numerical results and experiments. The species considered are electrons, singly-charged ions, neutrals at ground state, and excited (i.e., $1s_M$, $1s_R$, and $2p$).

The experimental set up consists of a 20 cm long source tube connected to a 28.8 cm long expansion chamber; diameters are 13.6 cm and 32 cm respectively. A double-saddle antenna, wrapped around the source tube, drives the discharge, and operates at 13.56 MHz. The argon base pressure is 3 mTorr. A magneto-static field of intensity up to 2.1 mT is generated by a coil near the exhaust of the source tube. From a numerical standpoint, the power deposition profile is calculated with the EM-module of 3D-VIRTUS⁴⁶. The fluid equations are solved in a 2D-axisymmetric domain consisting in a structured hexa-mesh of 11000 elements. For further de-

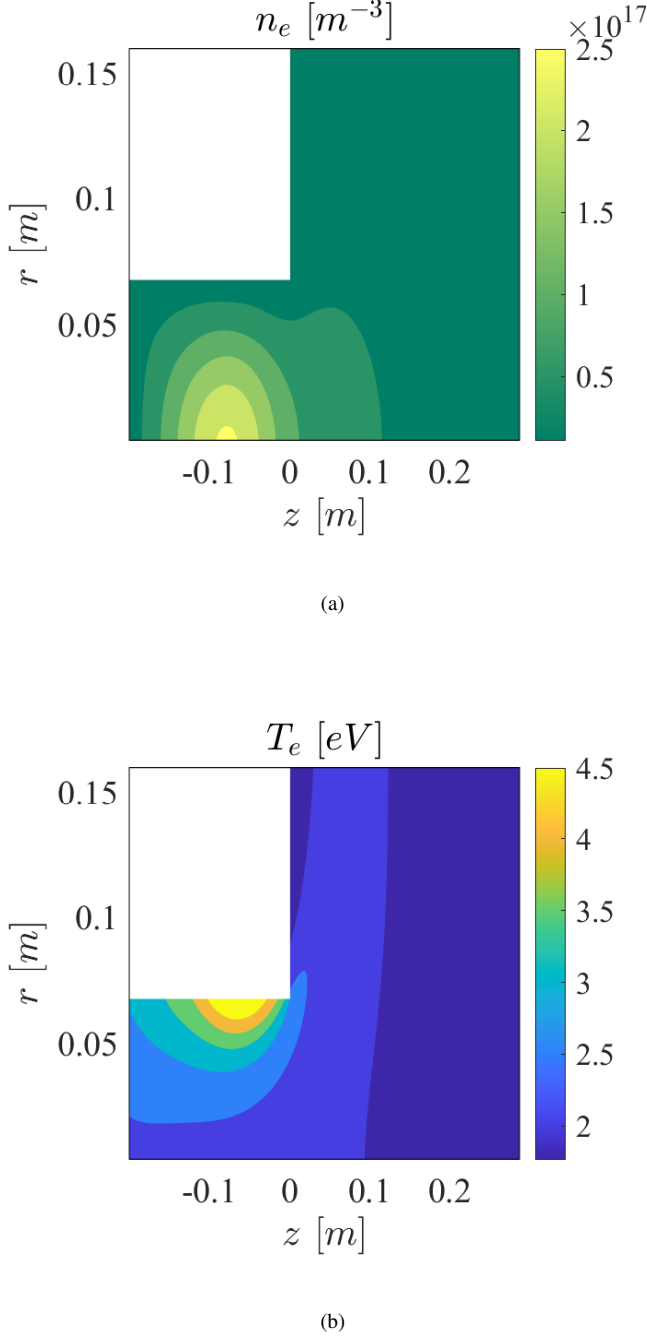


FIG. 12. Map of (a) electron density n_e and (b) electron temperature T_e as a function of radial and axial coordinates (r, z) for the highest density case.

tails on the experimental setup see Lafleur⁶⁰, for the numerical strategy refer to Magarotto⁴⁶ and Souhair⁵⁵.

In Fig. 11, numerical results are compared against experimental data; n_e is depicted as a function of the axial position within the reactor (the interface between the source and the expansion chamber is located at $z = 0$ m). The choice of the cross-section dataset does not influence the shape of

the plasma density profile but only its peak value. The measured one is $3.3 \times 10^{17} \text{ m}^{-3}$ whereas the numerical simulations provide a value comprised between $2.6 \times 10^{17} \text{ m}^{-3}$ and $2.15 \times 10^{17} \text{ m}^{-3}$. As expected, the numerical envelope presents a non-negligible variance of about 18%. Nonetheless, the numerical results match the experimental trend and the envelope overlaps the measurements uncertainty band which is 25% as discussed in Magarotto⁴⁶. Electron density and temperature maps are depicted in Fig. 12 for the highest density case. For what computation affordability is concerned, the average simulation time is about 15 minutes on a parallelized quad-core Intel machine. **This value is only 20% higher with respect to the time required to perform a less accurate simulation where the dynamics of only one effective excited species were solved⁴⁶. In conclusion the lumping procedure is demonstrated to provide accurate results and to be in general affordable for a multidimensional code.**

IV. CONCLUSIONS

This work addresses two main topics: (i) presenting a lumping strategy to account, in a reasonable computation time, for the dynamics of the excited states in neon, argon, krypton, and xenon low pressure (<50 mTorr) discharges; (ii) performing a sensitivity analysis to assess how cross-sections from different datasets affect the estimation of plasma parameters.

Regarding the first point, only $1s$ and $2p$ excited states have been simulated. The fine structure energy levels have been lumped in metastable and resonant $1s$ ($1s_M$ and $1s_R$ respectively), along with $2p$. The proposed methodology relies on the assumption that LTE holds between the fine structure energy states that are lumped together. Both collisional excitation/de-excitation and radiative decay reactions have been considered, so no assumption of LTE nor Corona equilibrium is done between different lumped states⁶⁴. The lumping methodology has been benchmarked against the results obtained treating all the excited states as separate species; differences lower than 1% have been registered. Experimental evaluations of the electron density and electron temperature have been used to validate the proposed methodology. Specifically an ICP reactor¹⁵ operated with argon, neon, krypton and xenon has been simulated with a *Global Model*. Subsequently, a Piglet reactor⁶⁰ operated with argon gas has been analysed with a 2D-axisymmetric fluid code. In both cases, a fairly good agreement between numerical and experimental results has been obtained (maximum disagreement 30%). Moreover, the computational affordability of the lumping strategy implemented in a fluid code has been proven by the simulation of a magnetized plasma.

Regarding the second point, the choice of the cross-section dataset can have a non-negligible effect on the results of the simulation, in particular if radiative decay is modelled. A maximum variance between highest and lowest density is 30%. A single set of cross-sections that gives results always closer to experiments has not been found. Therefore in Appendix A an analytical fitting of the rate coefficients that provide the highest and the lowest density for each gas has been

reported.

The main outcome of this work is a methodology to investigate, in a reasonable computation time, how the dynamics of the excited states affect the estimation of plasma density and temperature in low pressure discharges. The approach might be used in future works to accurately identify the transitions between excited states that have a major influence on the dynamics of the discharge¹⁰¹. At the same time, this methodology can be employed to verify the applicability of assumptions as the LTE or the Corona equilibrium.

ACKNOWLEDGMENTS

The authors are grateful to Dr. F. Bosi for having supported their work with helpful discussions and insights on collisional radiative models. Moreover, we acknowledge T4i S.p.a. for the support provided in the development of this work.

DATA AVAILABILITY

The data that support the findings of this study are available from the corresponding author upon reasonable request.

Appendix A: Fitting of the rate coefficients

The rate coefficients obtained from the cross-section datasets referring to the highest and lowest density cases (see Sec. III) have been fitted using a polynomial form that reads,

$$K(T_e) = \sum_{i=0}^n p_i T_e^i \quad (\text{A1})$$

With $n = 6$, Eq. (A1) holds true in the range $T_e = [1, 20]$ eV for both argon, neon, krypton and xenon. The fitting coefficients (p_i) refer to the collisional-radiative case; for the highest density they are reported in Tab. XVII-XX, for the lowest density in Tab. XXI-XXIV.

The inverse reactions (i.e., de-excitation) rate coefficients, can be computed using the PDB and assuming a Maxwellian EEDF. The rate coefficient formula can be expressed as⁵⁷:

$$K_{ji} = K_{ij} \frac{g_i}{g_j} \exp\left(\frac{U_j - U_i}{qT_e}\right) \quad (\text{A2})$$

TABLE XVII. Lumped rate coefficients fitting constants for the highest density case in argon.

Transition ^{ab}	p_6	p_5	p_4	p_3	p_2	p_1	p_0	Ref. ^c
$gs \rightarrow 1s_m$	5.127×10^{-23}	-5.266×10^{-21}	2.019×10^{-19}	-3.647×10^{-18}	2.973×10^{-17}	-5.543×10^{-17}	2.173×10^{-17}	82,83
$gs \rightarrow 1s_r$	-3.619×10^{-22}	1.990×10^{-20}	-3.379×10^{-19}	1.653×10^{-19}	4.994×10^{-17}	-1.256×10^{-16}	5.670×10^{-17}	82,83
$gs \rightarrow 2p$	-2.801×10^{-22}	1.408×10^{-20}	-1.841×10^{-19}	-1.287×10^{-18}	4.144×10^{-17}	-1.017×10^{-16}	4.653×10^{-17}	81
$1s_m \rightarrow 1s_r$	6.448×10^{-20}	-4.580×10^{-18}	1.301×10^{-16}	-1.891×10^{-15}	1.496×10^{-14}	-6.403×10^{-14}	1.443×10^{-13}	82,83
$1s_m \rightarrow 2p$	4.237×10^{-20}	-1.939×10^{-18}	1.204×10^{-17}	7.987×10^{-16}	-2.037×10^{-14}	2.320×10^{-13}	-7.235×10^{-14}	82,83
$1s_r \rightarrow 2p$	1.030×10^{-19}	-6.072×10^{-18}	1.228×10^{-16}	-6.799×10^{-16}	-1.011×10^{-14}	1.962×10^{-13}	-6.453×10^{-14}	82,83
$gs \rightarrow ion^d$	-6.207×10^{-21}	4.196×10^{-19}	-1.069×10^{-17}	1.179×10^{-16}	-3.352×10^{-16}	2.636×10^{-16}	-2.385×10^{-17}	81
$1s \rightarrow ion$	8.383×10^{-20}	-5.591×10^{-18}	1.441×10^{-16}	-1.762×10^{-15}	9.393×10^{-15}	-1.789×10^{-15}	-2.626×10^{-15}	95
$2p \rightarrow ion$	1.57×10^{-19}	-9.773×10^{-18}	2.254×10^{-16}	-2.218×10^{-15}	5.157×10^{-15}	5.868×10^{-14}	-3.014×10^{-14}	95
$0 \rightarrow 0^e$	1.255×10^{-19}	-8.225×10^{-18}	2.047×10^{-16}	-2.31×10^{-15}	9.416×10^{-15}	2.265×10^{-14}	-7.953×10^{-15}	81

^a Transitions refer to electronic collisional reactions.^b Reverse transitions shall be derived using the *Detailed Balance Principle*.^c Reference refer to the set of cross-sections considered for the actual lumped transition.^d Ionization by electron collision.^e Elastic scattering of neutral particles.

TABLE XVIII. Lumped rate coefficients fitting constants for the highest density case in neon.

Transition ^{ab}	p_6	p_5	p_4	p_3	p_2	p_1	p_0	Ref. ^c
$gs \rightarrow 1s_m$	-2.883×10^{-23}	1.588×10^{-21}	-2.782×10^{-20}	8.359×10^{-20}	1.912×10^{-18}	-5.746×10^{-18}	2.879×10^{-18}	82,83
$gs \rightarrow 1s_r$	-1.643×10^{-22}	1.086×10^{-20}	-2.686×10^{-19}	2.811×10^{-18}	-6.025×10^{-18}	8.802×10^{-19}	2.045×10^{-18}	82,83
$gs \rightarrow 2p$	-1.104×10^{-22}	7.115×10^{-21}	-1.691×10^{-19}	1.662×10^{-18}	-3.407×10^{-18}	-1.259×10^{-19}	1.638×10^{-18}	82,83
$1s_m \rightarrow 1s_r$	-	-	-	-	-	-	-	-
$1s_m \rightarrow 2p$	1.141×10^{-20}	5.107×10^{-19}	-6.216×10^{-17}	1.803×10^{-15}	-2.367×10^{-14}	1.500×10^{-13}	-5.824×10^{-14}	97
$1s_r \rightarrow 2p$	2.029×10^{-19}	-1.064×10^{-17}	1.635×10^{-16}	3.213×10^{-16}	-3.217×10^{-14}	3.097×10^{-13}	-1.293×10^{-13}	97
$gs \rightarrow ion^d$	-1.068×10^{-22}	1.109×10^{-20}	-4.296×10^{-19}	7.386×10^{-18}	-3.496×10^{-17}	5.561×10^{-17}	-2.115×10^{-17}	92
$1s \rightarrow ion$	5.721×10^{-20}	-3.886×10^{-18}	1.027×10^{-16}	-1.308×10^{-15}	7.525×10^{-15}	-5.076×10^{-15}	-1.139×10^{-16}	95
$2p \rightarrow ion$	1.55×10^{-19}	-9.868×10^{-18}	2.366×10^{-16}	-2.539×10^{-15}	9.265×10^{-15}	3.449×10^{-14}	-2.057×10^{-14}	95
$0 \rightarrow 0^e$	3.175×10^{-21}	-2.326×10^{-19}	6.23×10^{-18}	-6.628×10^{-17}	-4.102×10^{-17}	8.1×10^{-15}	2.857×10^{-15}	84

^a Transitions refer to electronic collisional reactions.^b Reverse transitions shall be derived using the *Detailed Balance Principle*.^c Reference refer to the set of cross-sections considered for the actual lumped transition.^d Ionization by electron collision.^e Elastic scattering of neutral particles.

TABLE XIX. Lumped rate coefficients fitting constants for the highest density case in krypton.

Transition ^{ab}	p_6	p_5	p_4	p_3	p_2	p_1	p_0	Ref. ^c
$gs \rightarrow 1s_m$	-3.508×10^{-21}	2.128×10^{-19}	-4.594×10^{-18}	3.683×10^{-17}	1.321×10^{-17}	-2.538×10^{-16}	1.614×10^{-16}	87
$gs \rightarrow 1s_r$	-1.840×10^{-22}	8.551×10^{-21}	-8.404×10^{-20}	-1.427×10^{-18}	2.823×10^{-17}	-7.101×10^{-17}	3.368×10^{-17}	87
$gs \rightarrow 2p$	-1.875×10^{-21}	9.642×10^{-20}	-1.419×10^{-18}	-2.471×10^{-18}	1.912×10^{-16}	-5.224×10^{-16}	2.553×10^{-16}	87
$1s_m \rightarrow 1s_r$	9.351×10^{-19}	-8.017×10^{-17}	2.737×10^{-15}	-4.757×10^{-14}	4.448×10^{-13}	-2.164×10^{-12}	4.700×10^{-12}	87
$1s_m \rightarrow 2p$	3.055×10^{-19}	-1.377×10^{-17}	1.018×10^{-16}	4.098×10^{-15}	-9.285×10^{-14}	7.405×10^{-13}	-3.020×10^{-13}	87
$1s_r \rightarrow 2p$	-1.042×10^{-18}	7.400×10^{-17}	-2.105×10^{-15}	3.074×10^{-14}	-2.462×10^{-13}	1.062×10^{-12}	-2.401×10^{-13}	87
$gs \rightarrow ion^d$	-9.064×10^{-21}	6.003×10^{-19}	-1.485×10^{-17}	1.549×10^{-16}	-3.252×10^{-16}	4.18×10^{-17}	1.116×10^{-16}	92
$1s \rightarrow ion$	9.019×10^{-20}	-5.965×10^{-18}	1.519×10^{-16}	-1.824×10^{-15}	9.332×10^{-15}	1.234×10^{-15}	-4.211×10^{-15}	95
$2p \rightarrow ion$	1.473×10^{-19}	-8.987×10^{-18}	1.997×10^{-16}	-1.788×10^{-15}	1.272×10^{-15}	7.632×10^{-14}	-3.633×10^{-14}	95
$0 \rightarrow 0^e$	1.417×10^{-19}	-8.708×10^{-18}	1.951×10^{-16}	-1.77×10^{-15}	2.165×10^{-15}	4.954×10^{-14}	-1.645×10^{-14}	90

^a Transitions refer to electronic collisional reactions.^b Reverse transitions shall be derived using the *Detailed Balance Principle*.^c Reference refer to the set of cross-sections considered for the actual lumped transition.^d Ionization by electron collision.^e Elastic scattering of neutral particles.

TABLE XX. Lumped rate coefficients fitting constants for the highest density case in xenon.

Transition ^{ab}	p_6	p_5	p_4	p_3	p_2	p_1	p_0	Ref. ^c
$gs \rightarrow 1s_m$	1.142×10^{-21}	-7.975×10^{-20}	2.172×10^{-18}	-2.846×10^{-17}	1.691×10^{-16}	-2.222×10^{-16}	6.016×10^{-17}	⁸⁰
$gs \rightarrow 1s_r$	-1.623×10^{-21}	8.309×10^{-20}	-1.096×10^{-18}	-9.582×10^{-18}	3.141×10^{-16}	-7.064×10^{-16}	3.025×10^{-16}	⁸⁰
$gs \rightarrow 2p$	7.969×10^{-22}	-6.896×10^{-20}	2.358×10^{-18}	-3.968×10^{-17}	3.146×10^{-16}	-5.489×10^{-16}	2.024×10^{-16}	⁸⁴
$1s_m \rightarrow 1s_r$	2.180×10^{-21}	-5.305×10^{-20}	-2.078×10^{-18}	9.470×10^{-17}	-1.348×10^{-15}	7.811×10^{-15}	-3.385×10^{-15}	³³
$1s_m \rightarrow 2p$	1.173×10^{-19}	-5.245×10^{-18}	4.148×10^{-17}	1.269×10^{-15}	-2.624×10^{-14}	1.791×10^{-13}	-8.287×10^{-14}	³³
$1s_r \rightarrow 2p$	-3.960×10^{-19}	3.060×10^{-17}	-9.637×10^{-16}	1.595×10^{-14}	-1.494×10^{-13}	7.833×10^{-13}	-2.225×10^{-13}	³³
$gs \rightarrow ion^d$	-1.182×10^{-20}	7.33×10^{-19}	-1.627×10^{-17}	1.32×10^{-16}	2.268×10^{-16}	-1.25×10^{-15}	6.844×10^{-16}	⁸⁴
$1s \rightarrow ion$	9.971×10^{-20}	-6.56×10^{-18}	1.657×10^{-16}	-1.963×10^{-15}	9.733×10^{-15}	4.011×10^{-15}	-5.768×10^{-15}	⁹⁵
$2p \rightarrow ion$	1.456×10^{-19}	-8.759×10^{-18}	1.894×10^{-16}	-1.564×10^{-15}	-1.27×10^{-15}	9.049×10^{-14}	-4.146×10^{-14}	⁹⁵
$0 \rightarrow 0^e$	-8.535×10^{-21}	2.448×10^{-18}	-1.339×10^{-16}	3.084×10^{-15}	-3.464×10^{-14}	1.795×10^{-13}	-4.371×10^{-14}	⁹¹

^a Transitions refer to electronic collisional reactions.^b Reverse transitions shall be derived using the *Detailed Balance Principle*.^c Reference refer to the set of cross-sections considered for the actual lumped transition.^d Ionization by electron collision.^e Elastic scattering of neutral particles.

TABLE XXI. Lumped rate coefficients fitting constants for the lowest density case in argon.

Transition ^{ab}	p_6	p_5	p_4	p_3	p_2	p_1	p_0	Ref. ^c
$gs \rightarrow 1s_m$	6.176×10^{-23}	-8.633×10^{-21}	3.823×10^{-19}	-7.465×10^{-18}	6.352×10^{-17}	-1.260×10^{-16}	5.194×10^{-17}	⁸⁵
$gs \rightarrow 1s_r$	-7.345×10^{-22}	3.842×10^{-20}	-5.515×10^{-19}	-2.677×10^{-18}	1.135×10^{-16}	-2.787×10^{-16}	1.260×10^{-16}	⁸⁵
$gs \rightarrow 2p$	-1.041×10^{-21}	5.698×10^{-20}	-9.819×10^{-19}	2.390×10^{-18}	8.000×10^{-17}	-2.298×10^{-16}	1.126×10^{-16}	⁷⁸
$1s_m \rightarrow 1s_r$	9.268×10^{-18}	-6.217×10^{-16}	1.637×10^{-14}	-2.141×10^{-13}	1.451×10^{-12}	-4.839×10^{-12}	6.733×10^{-12}	⁸⁷
$1s_m \rightarrow 2p$	-2.634×10^{-19}	1.891×10^{-17}	-5.383×10^{-16}	7.727×10^{-15}	-6.107×10^{-14}	3.320×10^{-13}	-1.008×10^{-13}	⁸⁷
$1s_r \rightarrow 2p$	-1.816×10^{-18}	1.266×10^{-16}	-3.503×10^{-15}	4.884×10^{-14}	-3.587×10^{-13}	1.301×10^{-12}	1.789×10^{-13}	⁸⁷
$gs \rightarrow ion^d$	-6.207×10^{-21}	4.196×10^{-19}	-1.069×10^{-17}	1.179×10^{-16}	-3.352×10^{-16}	2.636×10^{-16}	-2.385×10^{-17}	⁸¹
$1s \rightarrow ion$	8.383×10^{-20}	-5.591×10^{-18}	1.441×10^{-16}	-1.762×10^{-15}	9.393×10^{-15}	-1.789×10^{-15}	-2.626×10^{-15}	⁹⁵
$2p \rightarrow ion$	1.57×10^{-19}	-9.773×10^{-18}	2.254×10^{-16}	-2.218×10^{-15}	5.157×10^{-15}	5.868×10^{-14}	-3.014×10^{-14}	⁹⁵
$0 \rightarrow 0^e$	1.255×10^{-19}	-8.225×10^{-18}	2.047×10^{-16}	-2.31×10^{-15}	9.416×10^{-15}	2.265×10^{-14}	-7.953×10^{-15}	⁸¹

^a Transitions refer to electronic collisional reactions.^b Reverse transitions shall be derived using the *Detailed Balance Principle*.^c Reference refer to the set of cross-sections considered for the actual lumped transition.^d Ionization by electron collision.^e Elastic scattering of neutral particles.

TABLE XXII. Lumped rate coefficients fitting constants for the lowest density case in neon.

Transition ^{ab}	p_6	p_5	p_4	p_3	p_2	p_1	p_0	Ref. ^c
$gs \rightarrow 1s_m$	-4.778×10^{-23}	2.725×10^{-21}	-5.159×10^{-20}	2.55×10^{-19}	2.148×10^{-18}	-7.363×10^{-18}	3.825×10^{-18}	⁸⁴
$gs \rightarrow 1s_r$	-2.912×10^{-22}	1.958×10^{-20}	-4.937×10^{-19}	5.32×10^{-18}	-1.409×10^{-17}	9.289×10^{-18}	9.533×10^{-20}	⁸⁴
$gs \rightarrow 2p$	-2.177×10^{-22}	1.395×10^{-20}	-3.282×10^{-19}	3.17×10^{-18}	-6.683×10^{-18}	2.265×10^{-19}	2.942×10^{-18}	⁸⁴
$1s_m \rightarrow 1s_r$	-	-	-	-	-	-	-	-
$1s_m \rightarrow 2p$	1.141×10^{-20}	5.107×10^{-19}	-6.216×10^{-17}	1.803×10^{-15}	-2.367×10^{-14}	1.500×10^{-13}	-5.824×10^{-14}	⁹⁷
$1s_r \rightarrow 2p$	2.029×10^{-19}	-1.064×10^{-17}	1.635×10^{-16}	3.213×10^{-16}	-3.217×10^{-14}	3.097×10^{-13}	-1.293×10^{-13}	⁹⁷
$gs \rightarrow ion^d$	-1.068×10^{-22}	1.109×10^{-20}	-4.296×10^{-19}	7.386×10^{-18}	-3.496×10^{-17}	5.561×10^{-17}	-2.115×10^{-17}	⁹²
$1s \rightarrow ion$	5.721×10^{-20}	-3.886×10^{-18}	1.027×10^{-16}	-1.308×10^{-15}	7.525×10^{-15}	-5.076×10^{-15}	-1.139×10^{-16}	⁹⁵
$2p \rightarrow ion$	1.55×10^{-19}	-9.868×10^{-18}	2.366×10^{-16}	-2.539×10^{-15}	9.265×10^{-15}	3.449×10^{-14}	-2.057×10^{-14}	⁹⁵
$0 \rightarrow 0^e$	3.175×10^{-21}	-2.326×10^{-19}	6.23×10^{-18}	-6.628×10^{-17}	-4.102×10^{-17}	8.1×10^{-15}	2.857×10^{-15}	⁸⁴

^a Transitions refer to electronic collisional reactions.^b Reverse transitions shall be derived using the *Detailed Balance Principle*.^c Reference refer to the set of cross-sections considered for the actual lumped transition.^d Ionization by electron collision.^e Elastic scattering of neutral particles.

TABLE XXIII. Lumped rate coefficients fitting constants for the lowest density case in krypton.

Transition ^{ab}	p_6	p_5	p_4	p_3	p_2	p_1	p_0	Ref. ^c
$gs \rightarrow 1s_m$	-8.269×10^{-22}	4.356×10^{-20}	$-6. \times 10^{-19}$	-3.501×10^{-18}	1.523×10^{-16}	-3.435×10^{-16}	1.465×10^{-16}	82,83
$gs \rightarrow 1s_r$	-1.714×10^{-23}	-2.624×10^{-21}	2.038×10^{-19}	-4.925×10^{-18}	4.708×10^{-17}	-9.533×10^{-17}	3.981×10^{-17}	82,83
$gs \rightarrow 2p$	-4.624×10^{-22}	8.278×10^{-21}	6.258×10^{-19}	-2.335×10^{-17}	2.686×10^{-16}	-5.703×10^{-16}	2.434×10^{-16}	82,83
$1s_m \rightarrow 1s_r$	9.351×10^{-19}	-8.017×10^{-17}	2.737×10^{-15}	-4.757×10^{-14}	4.448×10^{-13}	-2.164×10^{-12}	4.700×10^{-12}	87
$1s_m \rightarrow 2p$	3.055×10^{-19}	-1.377×10^{-17}	1.018×10^{-16}	4.098×10^{-15}	-9.285×10^{-14}	7.405×10^{-13}	-3.020×10^{-13}	87
$1s_r \rightarrow 2p$	-1.042×10^{-18}	7.400×10^{-17}	-2.105×10^{-15}	3.074×10^{-14}	-2.462×10^{-13}	1.062×10^{-12}	-2.401×10^{-13}	87
$gs \rightarrow ion^d$	-9.242×10^{-21}	6.128×10^{-19}	-1.517×10^{-17}	1.586×10^{-16}	-3.418×10^{-16}	6.276×10^{-17}	1.062×10^{-16}	90
$1s \rightarrow ion$	9.019×10^{-20}	-5.965×10^{-18}	1.519×10^{-16}	-1.824×10^{-15}	9.332×10^{-15}	1.234×10^{-15}	-4.211×10^{-15}	95
$2p \rightarrow ion$	1.473×10^{-19}	-8.987×10^{-18}	1.997×10^{-16}	-1.788×10^{-15}	1.272×10^{-15}	7.632×10^{-14}	-3.633×10^{-14}	95
$0 \rightarrow 0^e$	1.452×10^{-19}	-8.848×10^{-18}	1.954×10^{-16}	-1.705×10^{-15}	6.815×10^{-16}	6.593×10^{-14}	-2.394×10^{-14}	91

^a Transitions refer to electronic collisional reactions.^b Reverse transitions shall be derived using the *Detailed Balance Principle*.^c Reference refer to the set of cross-sections considered for the actual lumped transition.^d Ionization by electron collision.^e Elastic scattering of neutral particles.

TABLE XXIV. Lumped rate coefficients fitting constants for the lowest density case in xenon.

Transition ^{ab}	p_6	p_5	p_4	p_3	p_2	p_1	p_0	Ref. ^c
$gs \rightarrow 1s_m$	1.011×10^{-21}	-7.411×10^{-20}	2.142×10^{-18}	-3.016×10^{-17}	1.957×10^{-16}	-2.820×10^{-16}	8.728×10^{-17}	83
$gs \rightarrow 1s_r$	-2.919×10^{-22}	-3.913×10^{-23}	7.914×10^{-19}	-2.665×10^{-17}	3.359×10^{-16}	-6.299×10^{-16}	2.421×10^{-16}	83
$gs \rightarrow 2p$	3.020×10^{-22}	-4.962×10^{-20}	2.422×10^{-18}	-5.217×10^{-17}	4.964×10^{-16}	-9.126×10^{-16}	3.487×10^{-16}	83
$1s_m \rightarrow 1s_r$	-1.029×10^{-19}	6.702×10^{-18}	-1.717×10^{-16}	2.220×10^{-15}	-1.537×10^{-14}	4.340×10^{-14}	2.880×10^{-13}	98
$1s_m \rightarrow 2p$	1.173×10^{-19}	-5.245×10^{-18}	4.148×10^{-17}	1.269×10^{-15}	-2.624×10^{-14}	1.791×10^{-13}	-8.287×10^{-14}	33
$1s_r \rightarrow 2p$	-3.960×10^{-19}	3.060×10^{-17}	-9.637×10^{-16}	1.595×10^{-14}	-1.494×10^{-13}	7.833×10^{-13}	-2.225×10^{-13}	33
$gs \rightarrow ion^d$	-1.201×10^{-20}	7.527×10^{-19}	-1.703×10^{-17}	1.461×10^{-16}	1.01×10^{-16}	-1.008×10^{-15}	5.883×10^{-16}	92
$1s \rightarrow ion$	9.971×10^{-20}	-6.56×10^{-18}	1.657×10^{-16}	-1.963×10^{-15}	9.733×10^{-15}	4.011×10^{-15}	-5.768×10^{-15}	95
$2p \rightarrow ion$	1.456×10^{-19}	-8.759×10^{-18}	1.894×10^{-16}	-1.564×10^{-15}	-1.27×10^{-15}	9.049×10^{-14}	-4.146×10^{-14}	95
$0 \rightarrow 0^e$	-8.535×10^{-21}	2.448×10^{-18}	-1.339×10^{-16}	3.084×10^{-15}	-3.464×10^{-14}	1.795×10^{-13}	-4.371×10^{-14}	91

^a Transitions refer to electronic collisional reactions.^b Reverse transitions shall be derived using the *Detailed Balance Principle*.^c Reference refer to the set of cross-sections considered for the actual lumped transition.^d Ionization by electron collision.^e Elastic scattering of neutral particles.

REFERENCES

- ¹F. F. Chen, "Helicon discharges and sources: a review," *Plasma Sources Science and Technology* **24**, 014001 (2015).
- ²M. A. Lieberman and A. J. Lichtenberg, *Principles of Plasma Discharges and Materials Processing*, ii ed., edited by Wiley (Wiley, 2005).
- ³D. Pavarin, F. Ferri, M. Manente, D. Curreli, Y. Guclu, D. Melazzi, D. Rondini, S. Suman, J. Carlsson, C. Bramanti, *et al.*, "Design of 50 W Helicon Plasma Thruster," in *The 31st International Electric Propulsion Conference IEPC-2009-205* (Ann Arbor, Michigan, USA, 2009).
- ⁴F. Trezzolani, M. Manente, A. Selmo, D. Melazzi, M. Magarotto, D. Moretto, P. De Carlo, M. Pessana, and D. Pavarin, "Development and test of an high power RF plasma thruster in project SAPERE-STRONG," in *The 35th International Electric Propulsion Conference IEPC-2017-462* (Atlanta, GA, USA, 2017).
- ⁵F. Trezzolani, M. Magarotto, M. Manente, and D. Pavarin, "Development of a counterbalanced pendulum thrust stand for electric propulsion," *Measurement* **122**, 494–501 (2018).
- ⁶F. Chang Diaz, J. P. Squire, M. Carter, A. Corrigan, L. Dean, J. Farrias, M. Giambusso, G. McCaskill, and T. Yao, "An Overview of the VASIMR® Engine," in *AIAA 2018-4416, 2018 Joint Propulsion Conference* (American Institute of Aeronautics and Astronautics, Reston, Virginia, 2018).
- ⁷J. Navarro-Cavallé, M. Wijnen, P. Fajardo, E. Ahedo, V. Gomez, A. Giménez, and M. Ruiz, "Development and Characterization of the Helicon Plasma Thruster Prototype HPT05M," in *The 36th International Electric Propulsion Conference IEPC-2019-596* (Vienna, Austria, 2019).
- ⁸N. Bellomo, M. Manente, F. Trezzolani, A. Gloder, A. Selmo, R. Mantellato, E. Toson, L. Cappellini, M. Duzzi, D. Scalzi, *et al.*, "Enhancement of microsatellites' mission capabilities: integration of REGULUS electric propulsion module into UniSat-7," in *Proceedings of the 70th International Astronautical Congress (IAC) 2019* (Washington D.C., 2019).
- ⁹M. Manente, F. Trezzolani, R. Mantellato, D. Scalzi, A. Schiavon, N. Souhair, M. Duzzi, L. Cappellini, A. Barbato, D. Paulon, *et al.*, "REGULUS: Iodine Fed Plasma Propulsion System for Small Satellites," in *The 36th International Electric Propulsion Conference IEPC-2019-417* (Vienna, Austria, 2019).
- ¹⁰M. Manente, F. Trezzolani, M. Magarotto, E. Fantino, A. Selmo, N. Bellomo, E. Toson, and D. Pavarin, "Regulus: A propulsion platform to boost small satellite missions," *Acta Astronautica* **157**, 241–249 (2019).
- ¹¹P. De Carlo, M. Magarotto, G. Mansutti, A. Selmo, A.-D. Capobianco, and D. Pavarin, "Feasibility study of a novel class of plasma antennas for SatCom navigation systems," *Acta Astronautica* **178**, 846–853 (2021).
- ¹²M. Magarotto, P. de Carlo, G. Mansutti, F. J. Bosi, N. E. Buris, A.-D. Capobianco, and D. Pavarin, "Numerical suite for gaseous plasma antennas simulation," *IEEE Transactions on Plasma Science* **49**, 285–297 (2021).
- ¹³A. Daykin-Iliopoulos, F. Bosi, F. Coccaro, M. Magarotto, A. Papadimopoulos, P. D. Carlo, C. Dobranszki, I. Golosnoy, and S. Gabriel, "Characterisation of a thermionic plasma source apparatus for high-density gaseous plasma antenna applications," *Plasma Sources Science and Technology* **29**, 115002 (2020).
- ¹⁴G. Mansutti, P. De Carlo, M. A. Hannan, F. Boulos, P. Rocca, A.-D. Capobianco, M. Magarotto, and A. Tuozzi, "Modeling and design of a plasma-based transmit-array with beam scanning capabilities," *Results in Physics* **16**, 102923 (2020).
- ¹⁵A. Schwabedissen, E. C. Benck, and J. R. Roberts, "Langmuir probe measurements in an inductively coupled plasma source," *Physical Review E* **55**, 3450–3459 (1997).
- ¹⁶D. M. Goebel and I. Katz, *Fundamentals of Electric Propulsion: Ion and Hall Thrusters*, edited by I. John Wiley Sons (John Wiley Sons, Inc., Hoboken, NJ, USA, 2008) pp. 1–507.
- ¹⁷M. Magarotto, D. Melazzi, and D. Pavarin, "Study on the influence of the magnetic field geometry on the power deposition in a helicon plasma source," *Journal of Plasma Physics* **85** (2019).
- ¹⁸G. Gallina, M. Magarotto, M. Manente, and D. Pavarin, "Enhanced bidimensional pic: An electrostatic/magnetostatic particle-in-cell code for plasma based systems," *Journal of Plasma Physics* **85** (2019).
- ¹⁹H. Kuninaka and S. Satori, "Development and Demonstration of a Cathodeless Electron Cyclotron Resonance Ion Thruster," *Journal of Propulsion and Power* **14**, 1022–1026 (1998).
- ²⁰E. Y. Choueiri and J. K. Ziemer, "Quasi-Steady Magnetoplasmadynamic Thruster Performance Database," *Journal of Propulsion and Power* **17**, 967–976 (2001).
- ²¹Z. Navrátil, D. Trunec, V. Hrachová, and A. Kanka, "Collisional-radiative model of neon discharge: determination of E / N in the positive column of low pressure discharge," *Journal of Physics D: Applied Physics* **40**, 1037–1046 (2007).
- ²²P. G. Hill and C. R. Peterson, *Mechanics And Thermodynamics of Propulsion* (Pearson, 1992) p. 754.
- ²³B. D. Prince, R. J. Bemish, and Y.-H. Chiu, "Emission-Excitation Cross Sections Relevant to Krypton-Propelled Electric Thrusters," *Journal of Propulsion and Power* **31**, 725–736 (2015).
- ²⁴L. S. Gangwar, R. K. Sharma, "Argon plasma modeling with detailed fine-structure cross sections," *Journal of Applied Physics* (2012), 10.1063/1.3693043.
- ²⁵A. Bogaerts, R. Gijbels, and J. Vlcek, "Collisional-radiative model for an argon glow discharge," *Journal of Applied Physics* **84**, 121–136 (1998).
- ²⁶J. Vlcek, "A collisional-radiative model applicable to argon discharges over a wide range of conditions. I. Formulation and basic data," *Journal of Physics D: Applied Physics* **22**, 623–631 (1989).
- ²⁷K. Katsonis and H. Drawin, "Transition probabilities for argon(I)," *Journal of Quantitative Spectroscopy and Radiative Transfer* **23**, 1–55 (1980).
- ²⁸J. Vlcek and V. Pelikan, "A collisional-radiative model applicable to argon discharges over a wide range of conditions. II. Application to low-pressure, hollow-cathode arc and low-pressure glow discharges," *Journal of Physics D: Applied Physics* **22**, 632–643 (1989).
- ²⁹J. Vlcek and V. Pelikan, "A collisional-radiative model applicable to argon discharges over a wide range of conditions. III. Application to atmospheric and subatmospheric pressure arcs," *Journal of Physics D: Applied Physics* **23**, 526–532 (1990).
- ³⁰X.-M. Zhu and Y.-K. Pu, "A simple collisional-radiative model for low-temperature argon discharges with pressure ranging from 1 pa to atmospheric pressure: kinetics of paschen 1s and 2p levels," *Journal of Physics D: Applied Physics* **43**, 015204 (2009).
- ³¹S. S. Baghel, S. Gupta, R. K. Gangwar, and R. Srivastava, "Diagnostics of low-temperature neon plasma through a fine-structure resolved collisional-radiative model," *Plasma Sources Science and Technology* **28**, 115010 (2019).
- ³²R. K. Gangwar, Dipti, R. Srivastava, and L. Stafford, "Spectroscopic diagnostics of low-pressure inductively coupled Kr plasma using a collisional-radiative model with fully relativistic cross sections," *Plasma Sources Science and Technology* **25**, 035025 (2016).
- ³³Priti, R. K. Gangwar, and R. Srivastava, "Collisional-radiative model of xenon plasma with calculated electron-impact fine-structure excitation cross-sections," *Plasma Sources Science and Technology* **28**, 025003 (2019).
- ³⁴X.-M. Zhu, Y.-F. Wang, Y. Wang, D.-R. Yu, O. Zatsarinny, K. Bartschat, T. V. Tsankov, and U. Czarnetzki, "A xenon collisional-radiative model applicable to electric propulsion devices: II. Kinetics of the 6 s , 6 p , and 5 d states of atoms and ions in Hall thrusters," *Plasma Sources Science and Technology* **28**, 105005 (2019).
- ³⁵B. D. Van Sijde, J. J. A. M. van der Mullen, and D. C. Schram, "Collisional Radiative Models in Plasmas," *Beiträge aus der Plasmaphysik* **24**, 447–473 (1984).
- ³⁶J. van Dijk, G. M. W. Kroesen, and A. Bogaerts, "Plasma modelling and numerical simulation," *Journal of Physics D: Applied Physics* **42**, 190301 (2009).
- ³⁷H. C. Kim, F. Iza, S. S. Yang, M. Radmilović-Radjenović, and J. K. Lee, "Particle and fluid simulations of low-temperature plasma discharges: benchmarks and kinetic effects," *Journal of Physics D: Applied Physics* **38**, R283–R301 (2005).
- ³⁸G. J. M. Hagelaar, J. Bareilles, L. Garrigues, and J. P. Boeuf, "Two-dimensional model of a stationary plasma thruster," *Journal of Applied Physics* **91**, 5592–5598 (2002).
- ³⁹I. G. Mikelides, I. Katz, D. M. Goebel, and J. E. Polk, "Hollow cathode theory and experiment. II. A two-dimensional theoretical model of the emitter region," *Journal of Applied Physics* **98**, 113303 (2005).

- ⁴⁰H. C. Dragnea, A. L. Ortega, H. Kamhawi, and I. D. Boyd, "Simulation of a Hall Effect Thruster Using Krypton Propellant," *Journal of Propulsion and Power* **36**, 335–345 (2020).
- ⁴¹J. D. Bukowski, D. B. Graves, and P. Vitello, "Two-dimensional fluid model of an inductively coupled plasma with comparison to experimental spatial profiles," *Journal of Applied Physics* **80**, 2614–2623 (1996).
- ⁴²D. Bose, T. Govindan, and M. Meyyappan, "Modeling of a helicon plasma source," *IEEE Transactions on Plasma Science* **31**, 464–470 (2003).
- ⁴³R. L. Kinder and M. J. Kushner, "Wave propagation and power deposition in magnetically enhanced inductively coupled and helicon plasma sources," *Journal of Vacuum Science Technology A: Vacuum, Surfaces, and Films* **19**, 76–86 (2001).
- ⁴⁴Á. Sánchez-Villar, J. Zhou, E. Ahedo, and M. Merino, "Coupled plasma transport and electromagnetic wave simulation of an ECR thruster," *Plasma Sources Science and Technology* **30**, 045005 (2021).
- ⁴⁵J. Zhou, D. Pérez-Grande, P. Fajardo, and E. Ahedo, "Numerical treatment of a magnetized electron fluid model within an electromagnetic plasma thruster simulation code," *Plasma Sources Science and Technology* **28**, 115004 (2019).
- ⁴⁶M. Magarotto, D. Melazzi, and D. Pavarin, "3D-VIRTUS: Equilibrium condition solver of radio-frequency magnetized plasma discharges for space applications," *Computer Physics Communications* **247**, 106953 (2020).
- ⁴⁷M. Magarotto, M. Manente, F. Trezzolani, and D. Pavarin, "Numerical model of a helicon plasma thruster," *IEEE Transactions on Plasma Science* **48**, 835–844 (2020).
- ⁴⁸S. Ashida, C. Lee, and M. A. Lieberman, "Spatially averaged (global) model of time modulated high density argon plasmas," *Journal of Vacuum Science & Technology A* **13**, 2498–2507 (1995), <https://doi.org/10.1116/1.579494>.
- ⁴⁹E. Suetomi, M. Tanaka, S. Kamiya, S. Hayashi, S. Ikeda, H. Sugawara, and Y. Sakai, "Two-dimensional fluid simulation of plasma reactors for the immobilization of krypton," *Computer Physics Communications* **125**, 60–74 (2000).
- ⁵⁰J. Meunier, P. Belenguer, and J. P. Boeuf, "Numerical model of an ac plasma display panel cell in neon-xenon mixtures," *Journal of Applied Physics* **78**, 731–745 (1995).
- ⁵¹L. C. Pitchford, L. L. Alves, K. Bartschat, S. F. Biagi, M. C. Bordage, A. V. Phelps, C. M. Ferreira, G. J. M. Hagelaar, W. L. Morgan, S. Pancheshnyi, *et al.*, "Comparisons of sets of electron-neutral scattering cross sections and swarm parameters in noble gases: I. Argon," *Journal of Physics D: Applied Physics* **46**, 334001 (2013).
- ⁵²M. C. Bordage, S. F. Biagi, L. L. Alves, K. Bartschat, S. Chowdhury, L. C. Pitchford, G. J. M. Hagelaar, W. L. Morgan, V. Puech, and O. Zatsarinny, "Comparisons of sets of electron-neutral scattering cross sections and swarm parameters in noble gases: III. Krypton and xenon," *Journal of Physics D: Applied Physics* **46**, 334003 (2013).
- ⁵³L. L. Alves, K. Bartschat, S. F. Biagi, M. C. Bordage, L. C. Pitchford, C. M. Ferreira, G. J. M. Hagelaar, W. L. Morgan, S. Pancheshnyi, A. V. Phelps, *et al.*, "Comparisons of sets of electron-neutral scattering cross sections and swarm parameters in noble gases: II. Helium and neon," *Journal of Physics D: Applied Physics* **46**, 334002 (2013).
- ⁵⁴P. Miller, G. Hebner, K. Greenberg, P. Pochan, and B. Aragon, "An Inductively-Coupled Plasma Source for the Gaseous Electronics Conference Rf Reference Cell," *Journal of Research of the National Institute of Standards and Technology* **100**, 427 (1995).
- ⁵⁵N. Souhair, M. Magarotto, M. Manente, D. Pavarin, and F. Ponti, "Improvement of a numerical tool for the simulation of a helicon plasma thruster," in *Proceedings of the 7th Space Propulsion Conference SP2020-00070* (Estoril, Portugal, 2021).
- ⁵⁶T. Lafleur, C. Charles, and R. W. Boswell, "Characterization of a helicon plasma source in low diverging magnetic fields," *Journal of Physics D: Applied Physics* **44**, 055202 (2011).
- ⁵⁷K. E. Evdokimov, M. E. Konischev, V. F. Pichugin, and Z. Sun, "Study of argon ions density and electron temperature and density in magnetron plasma by optical emission spectroscopy and collisional-radiative model," *Resource-Efficient Technologies* **3**, 187–193 (2017).
- ⁵⁸X.-M. Zhu and Y.-K. Pu, "A simple collisional-radiative model for low-pressure argon discharges," *Journal of Physics D: Applied Physics* **40**, 2533–2538 (2007).
- ⁵⁹"The national institute of standards and technology - atomic spectra database," <https://www.nist.gov/pml/atomic-spectra-database>, accessed on 1 January 2021.
- ⁶⁰T. Lafleur, C. Charles, and R. W. Boswell, "Characterization of a helicon plasma source in low diverging magnetic fields," *Journal of Physics D: Applied Physics* **44**, 055202 (2011).
- ⁶¹K. Takahashi, A. Chiba, A. Komuro, and A. Ando, "Axial Momentum Lost to a Lateral Wall of a Helicon Plasma Source," *Physical Review Letters* **114**, 195001 (2015).
- ⁶²G. J. M. Hagelaar and L. C. Pitchford, "Solving the Boltzmann equation to obtain electron transport coefficients and rate coefficients for fluid models," *Plasma Sources Science and Technology* **14**, 722–733 (2005).
- ⁶³R. Mewe, "Relative intensity of helium spectral lines as a function of electron temperature and density," *British Journal of Applied Physics* **18**, 107–118 (1967).
- ⁶⁴R. H. Huddleston and S. L. Leonard, *Physics Today*, 9 (Academic Press; 1st edition (January 1, 1965), 1966).
- ⁶⁵F. J. Bosi, "Global model of microwave plasma assisted N₂O dissociation for monopropellant propulsion," *Physics of Plasmas* **26**, 033510 (2019).
- ⁶⁶E. Ahedo and V. De Pablo, "Combined effects of electron partial thermalization and secondary emission in hall thruster discharges," *Physics of Plasmas* **14**, 083501 (2007).
- ⁶⁷P. C. Stangeby, "The plasma sheath," in *Physics of Plasma-Wall Interactions in Controlled Fusion* (Springer, 1986) pp. 41–97.
- ⁶⁸T.-T. Wang, J. Ma, and Z.-A. Wei, "Effect of electron reflection on magnetized plasma sheath in an oblique magnetic field," *Physics of Plasmas* **22**, 093505 (2015).
- ⁶⁹S. Barral, K. Makowski, Z. Peradzynski, N. Gascon, and M. Dudeck, "Wall material effects in stationary plasma thrusters. ii. near-wall and in-wall conductivity," *Physics of Plasmas* **10**, 4137–4152 (2003).
- ⁷⁰F. Taccogna, S. Longo, and M. Capitelli, "Plasma sheaths in hall discharge," *Physics of plasmas* **12**, 093506 (2005).
- ⁷¹F. J. Bosi, "Development of global models of plasma systems for space propulsion," PhD thesis (2016).
- ⁷²M. Magarotto and D. Pavarin, "Parametric Study of a Cathode-Less Radio Frequency Thruster," *IEEE Transactions on Plasma Science* **48**, 2723–2735 (2020).
- ⁷³G. J. M. Hagelaar, F. J. de Hoog, and G. M. W. Kroesen, "Boundary conditions in fluid models of gas discharges," *Physical Review E* **62**, 1452–1454 (2000).
- ⁷⁴W. Yang, S. N. Averkin, A. V. Khrabrov, I. D. Kaganovich, Y.-N. Wang, S. Aleiferis, and P. Svarnas, "Benchmarking and validation of global model code for negative hydrogen ion sources articles you may be interested in," *Phys. Plasmas* **25**, 113509 (2018).
- ⁷⁵J. Carlsson, A. Khrabrov, I. Kaganovich, T. Sommerer, and D. Keating, "Validation and benchmarking of two particle-in-cell codes for a glow discharge," *Plasma Sources Science and Technology* **26**, 014003 (2016).
- ⁷⁶M. M. Turner, A. Derzsi, Z. Donkó, D. Eremin, S. J. Kelly, T. Lafleur, and T. Mussenbrock, "Simulation benchmarks for low-pressure plasmas: Capacitive discharges," *Physics of Plasmas* **20**, 013507 (2013).
- ⁷⁷A. Berthelot and A. Bogaerts, "Modeling of plasma-based CO₂ conversion: lumping of the vibrational levels," *Plasma Sources Science and Technology* **25**, 045022 (2016).
- ⁷⁸L. L. Alves, "The IST-LISBON database on LXCat," *Journal of Physics: Conference Series* **565**, 012007 (2014).
- ⁷⁹TRINITI Database, Available online: <https://www.lxcat.net/TRINITI> (Accessed on 1 January 2021).
- ⁸⁰PUECH Database, Available online: <https://www.lxcat.net/Puech> (Accessed on 1 January 2021).
- ⁸¹HAYASHI Database, Available online: <https://www.lxcat.net/Hayashi> (Accessed on 1 January 2021).
- ⁸²O. Zatsarinny and K. Bartschat, "B-spline Breit-Pauli R-matrix calculations for electron collisions with argon atoms," *Journal of Physics B: Atomic, Molecular and Optical Physics* **37**, 4693–4706 (2004).
- ⁸³M. Allan, O. Zatsarinny, and K. Bartschat, "Near-threshold absolute angle-differential cross sections for electron-impact excitation of argon and xenon," *Phys. Rev. A* **74**, 030701 (2006).
- ⁸⁴BIAGI V8.97 Database, Available online: <https://www.lxcat.net/Biagi> (Accessed on 1 January 2021).

- ⁸⁵M. A. Khakoo, P. Vandeventer, J. G. Childers, I. Kanik, C. J. Fontes, K. Bartschat, V. Zeman, D. H. Madison, S. Saxena, R. Srivastava, and A. D. Stauffer, "Electron impact excitation of the argon 3p54s configuration: differential cross-sections and cross-section ratios," *Journal of Physics B: Atomic, Molecular and Optical Physics* **37**, 247–281 (2003).
- ⁸⁶J. E. Chilton, J. B. Boffard, R. S. Schappe, and C. C. Lin, "Measurement of electron-impact excitation into the 3p5-4p levels of argon using Fourier-transform spectroscopy," *Physical Review A* **57**, 267–277 (1998).
- ⁸⁷NGFSRDW Database, Available online: <https://www.lxcat.net/NGFSRDW> (Accessed on 1 January 2021).
- ⁸⁸O. Zatsarinny and K. Bartschat, "B-spline calculations of oscillator strengths in neutral argon," *Journal of Physics B: Atomic, Molecular and Optical Physics* **39**, 2145–2158 (2006).
- ⁸⁹J. B. Boffard, G. A. Piech, M. F. Gehrke, L. W. Anderson, and C. C. Lin, "Measurement of electron-impact excitation cross sections out of metastable levels of argon and comparison with ground-state excitation," *Physical Review A* **59**, 2749–2763 (1999).
- ⁹⁰MORGAN Database, Available online: <https://www.lxcat.net/Morgan> (Accessed on 1 January 2021).
- ⁹¹COP Database, Available online: <https://www.lxcat.net/COP> (Accessed on 1 January 2021).
- ⁹²BIAGI v7 Database, Available online: <https://www.lxcat.net/Biagi-v7.1> (Accessed on 1 January 2021).
- ⁹³PHHELPS Database, Available online: <https://www.lxcat.net/Phelps> (Accessed on 1 January 2021).
- ⁹⁴SIGLO Database, Available online: <https://www.lxcat.net/SIGLO> (Accessed on 1 January 2021).
- ⁹⁵H. A. Hyman, "Electron-impact ionization cross sections for excited states of the rare gases (ne, ar, kr, xe), cadmium, and mercury," *Phys. Rev. A* **20**, 855–859 (1979).
- ⁹⁶H. Deutsch, K. Becker, A. Grum-Grzhimailo, K. Bartschat, H. Summers, M. Probst, S. Matt-Leubner, and T. Märk, "Calculated cross sections for the electron-impact ionization of excited argon atoms using the DM formalism," *International Journal of Mass Spectrometry* **233**, 39–43 (2004).
- ⁹⁷S. S. Baghel, S. Gupta, R. K. Gangwar, and R. Srivastava, "Diagnostics of low-temperature neon plasma through a fine-structure resolved collisional-radiative model," *Plasma Sources Science and Technology* **28**, 115010 (2019).
- ⁹⁸T. J. Sommerer, "Model of a weakly ionized, low-pressure xenon dc positive column discharge plasma," *Journal of Physics D: Applied Physics* **29**, 769–778 (1996).
- ⁹⁹P. Grondein, T. Lafleur, P. Chabert, and A. Aanesland, "Global model of an iodine gridded plasma thruster," *Physics of Plasmas* **23**, 033514 (2016).
- ¹⁰⁰D. L. Crintea, U. Czarnetzki, S. Iordanova, I. Koleva, and D. Luggenhölscher, "Plasma diagnostics by optical emission spectroscopy on argon and comparison with Thomson scattering," *Journal of Physics D: Applied Physics* **42**, 045208 (2009).
- ¹⁰¹R. Zorat and D. Vender, "Global model for an rf hydrogen inductive plasma discharge in the deuterium negative ion source experiment including negative ions," *Journal of Physics D: Applied Physics* **33**, 1728 (2000).